https://doi.org/10.5194/essd-2022-292
Preprint. Discussion started: 29 September 2022

Open Access Earth System Science Data Discussions

Refining the resolution of DUACS along track (level 3) altimeter Sea Level products

Marie-Isabelle Pujol[1], Stéphanie Dupuy[1], Oscar Vergara[1], Antonio Sánchez-Román[2], Yannice Faugere[1], Pierre. Prandi[1], Mei-Ling Dabat[1], Quentin Dagneaux[1], Marine Lievin[1], Emeline Cadier[1], Gérald Dibarboure[3], Nicolas Picot[3]

[1]CLS, 11 rue Hermès, Parc Technologique du Canal, 31520 Ramonville St Agne, France
[2]IMEDEA, C/Miquel Marquès, 21 – 07190 Esporles – Illes Balears, Spain
[3]CNES, 18 avenue Edouard Belin, 31401 Toulouse Cedex 9, France

Correspondence to: M-I Pujol (mpujol@groupcls.com)

https://doi.org/10.5194/essd-2022-292
Preprint. Discussion started: 29 September 2022

Open Access Earth System Science Data Discussions

Abstract

This paper describes a high-resolution Level-3 (L3) altimeter Data Unification and Altimeter Combination System (DUACS) experimental regional product developed with support from the French space agency (CNES). Deduced from full rate (20Hz to 40Hz) Level-2 (L2) altimeter measurements, this product delivers Sea Level Anomalies (SLA) and other essential physical variables with a nearly 1-Km sampling over the North Atlantic 0cean. It allows us to resolve wavelengths from ~35 km to ~55Km depending on the altimeter considered. This was made possible by recent advances in radar altimeter processing for both Synthetic aperture Radar (SAR) and Low-Resolution Mode (LRM) measurements, and improvements made to different stages of the DUACS processing chain. Firstly, the new adaptive and LR-RMC (Low Resolution with Range Migration Correction) processing techniques were considered for Jason and Sentinel-3 (S3A) respectively. They significantly reduce errors at short wavelengths and, for the adaptive processing, possible land contamination near the coast. Next, up-to-date geophysical and environmental corrections were selected for this production. This includes specific corrections intended to reduce the measurement noise on LRM measurement and thus enhance the observability at short wavelengths. Compared to the 1Hz product, the observable wavelength reached with the experimental high-resolution product are reduced by up to one third, or up to half in the North-East Atlantic region. The residual noises were optimally filtered from full rate measurements taking into consideration the different observing capabilities of the altimeters processed. A specific data recovery strategy was applied, significantly optimizing the data availability both in the coastal and open ocean. This experimental L3 product is thus better resolved than the conventional 1Hz product, especially near the coast where it is defined up to ~5km against ~10km for the 1Hz version. The multi-mission cross-calibration processing was also optimized with an improved Long Wavelengths Error (LWE) correction leading to a better consistency between tracks with an 9-15% reduction of SLA variance at cross-over. The experimental L3 product improves the overall consistency with tide gauge measurements with a reduction of the variance of the SLA differences by 5 and 17% compared to the 1Hz product from S3A and Jason-3 (J3) measurements respectively. Primarily intended for regional applications, this product can significantly contribute to improving high resolution numerical model outputs via data assimilation. It also opens new perspectives for a better understanding of regional sea surface dynamics, with an improved representation of the coastal currents and a refined spectral content that reveals the unbalanced signal.

Introduction

As part of the CNES/SALP (Centre National d'Etudes Spatiales/Service d'Altimetrie et Localisation Precise) project, and the Copernicus Marine Environment and Monitoring Service (CMEMS), the DUACS system produces high quality multi-mission altimetry sea level products for oceanographic applications, climate forecasting centers, geophysics and biology communities. These products consist of directly usable and easy to manipulate Level-3 (L3; along-track cross-calibrated sea surface height) and Level-4 (L4; multiple sensors merged as maps or time series) products. They are widely used for different applications, including assimilation in numerical models. In past years, the DUACS products have been regularly updated in order to deliver products of the highest quality, based on the state of the art processing and corrections, and newly available measurements (Le Traon et al., 1998; Ducet et al., 2000; Dibarboure et al., 2011; Pujol et al., 2016; Taburet et al., 2019). Despite these evolutions, the effective resolution of the DUACS altimeter products remains low with regard to the new requirements made by different applications (Benveniste et al., 2019; Dufau et al., 2011; Mercator Ocean and CMEMS partners, 2017; SWOT NASA/JPL Project, 2018)

https://doi.org/10.5194/essd-2022-292
Preprint. Discussion started: 29 September 2022

Indeed, different advances in the small to sub mesoscale sea surface dynamical processes have given new insight into the importance of this signal in the ocean's dynamics (Ferrari and Wunsch, 2008; Rocha et al., 2016; Capet et al., 2008; Klein et al., 2008; Su et al., 2018). At the same time, the monitoring of sea level changes in coastal areas is an important societal issue. Because they allow synoptic monitoring of the signal over the global ocean, including coasts, altimeter measurement contributions are fundamental for both sub-mesoscale and coastal applications.

The processing of altimeter data thus now faces a new challenge in being able to accurately process the signal at yet finer spatial scales than hitherto considered. This issue will be even more critical for future altimeter missions such as the large swath SWOT (Surface Water and Ocean Topography) mission. In the same way, altimeter measurement processing needs to evolve in order to better resolve the signal in coastal areas. Meanwhile, users and more particularly modelers are also upgrading their models to resolve small-scale processes at regional scale. To this end, they will need to prepare their systems for the assimilation and propagation of the finer scale structures observed.

The land contamination affecting both altimeter radar and radiometer measurement, associated with degradation of the different corrections that need to be applied to altimeter measurements, and predominance of residual errors at short wavelengths have significantly reduced the quality of the altimeter products for such applications for many years (e.g. Dibarboure et al., 2014; Vignudelli et al., 2011).

Nevertheless, over the last decade, significant improvements have been made in the estimation of different geophysical corrections. Advances in atmospheric and barotropic ocean models have allowed more accurate correction of the ocean response to wind and pressure forcing (e.g. Carrère and Lyard, 2003); progress in modeling and assimilation techniques have contributed to more accurate barotropic ocean tide corrections (e.g. Lyard et al., 2021); new model corrections have also emerged and have allowed us to correct part of the coherent internal gravity wave signal (e.g. Zaron, 2019); tropospheric corrections, enhanced in coastal areas, are also available (e.g. Fernandes and Lázaro, 2016; Obligis et al., 2011); and progress has also been made in the determination of the Mean Sea Surface (MSS) field, still a fundamental part of altimeter data processing (Dibarboure and Pujol, 2021; Sandwell et al., 2017)

Major advances made in altimeter technologies and processing have also significantly contributed to reducing altimeter measurement errors. First the Ka band used for SARAL/Altika significantly reduced the measurement noise on conventional LRM altimetry (Verron et al., 2018). For a few years already, the SAR technology available on the Cryosat-2 (C2) and Sentinel-3 missions has also contributed to an unprecedented reduction of the observational errors at short wavelengths (e.g. Cotton et al., 2015; Raynal et al., 2018). New processing techniques have been developed to enhance SAR capabilities and reduce residual red noise induced by long ocean waves (Boy et al., 2017; Egido and Smith, 2017; Moreau et al., 2021). In the same way, new waveform retracking techniques have allowed us to reduce residual noise levels on LRM measurements and even better adapt the model to the waveform shape characteristic of different sea surface states and land/ice contamination (Gommenginger et al., 2010; Passaro et al., 2014; Sandwell and Smith, 2005; Thibaut et al., 2017). Recent progress made in sea state bias correction have also contributed to reducing the measurement noise (Passaro et al., 2018; Tran et al., 2021). Additionally, corrections have been developed to specifically reduce signal noise at short wavelengths (Quartly et al., 2019; Quilfen and Chapron, 2021; Tran et al., 2021; Zaron and deCarvalho, 2016).

In light of these developments and the associated reduction of the errors at short wavelengths, the full rate altimeter measurement can now be used to access the small mesoscale signal and better sample difficult areas

https://doi.org/10.5194/essd-2022-292
Preprint. Discussion started: 29 September 2022

such as coastal zones or leads. Different regional altimeter products have been developed over the last few years with the aim of focusing on the coastal zone (e.g. PISTACH (Mercier et al., 2010); X-TRACK (Birol et al., 2017; Roblou et al., 2011); X-TRACK-ALES (Birol et al., 2021), ESA EO4SIBS (Grégoire and EO4SIBS consortium (ESA project), 2021)). Others are dedicated to ice-contaminated areas, focusing on the sea surface over leads (Auger et al., 2022; Prandi et al., 2021). In this paper we focus on the DUACS high resolution L3 altimeter experimental regional products, primarily intended for high resolution regional model applications and guided by the CMEMS requirements. These products have been developed in a CNES R&D context with the aim of preparing the future generation of L3 altimeter products that may be disseminated operationally in the CMEMS catalogue. In contrast with the current 1Hz L3 product available in CMEMS, this new L3 product is defined with a 5Hz sampling rate and derived from high resolution (20Hz) altimeter measurement specifically processed in order to better resolve finer scales down to ~35 km.

The paper is organized as follows: In section 1, the processing and different corrections used are described. Section 2 focusses on the data validation while some use cases are given in section 3. Essential information to assess and use the new L3 product is given in section 4. Lastly, a summary and conclusion are drawn in section 5.

1. Data processing

1.1. DUACS processing overview

The processing used for the high sampling L3 altimeter is based on the DUACS system. Originally developed for processing the 1Hz upstream altimeter measurements (Dibarboure et al., 2011; Ducet et al., 2000; Le Traon et al., 1998; Pujol et al., 2016; Taburet et al., 2019), the system has here been specifically adapted for the processing of full-rate (20 to 40Hz) upstream products. The method is essentially the same as that for the historical 1Hz production. It consists of the following steps: acquisition; homogenization; input data quality control; cross-calibration; along-track L3 product generation and final quality control as fully described in (Pujol et al., 2016). However, some algorithms have been reviewed to fit the full rate measurement constraints.

First, the different altimeter standards and corrections applied were selected in order to reduce the measurement noise as much as possible, as it is a lot higher for 20Hz measurements than for 1Hz (see section 1.2). This step is necessary if we want to explore the small mesoscale. Then, the data recovery strategy was reviewed using data selection criteria fitted to the full-rate signal characteristics and using metrics available at full-rate resolution (see section 1.3). The cross-calibration between missions was also improved (see section 1.5). A final low-pass filtering was applied to the SLA in order to reduce the residual noise and at the same time keep as much as possible of the physical signal at small wavelengths (see section 1.4). The L3 along-track products are delivered at a 5Hz (i.e. nearly 1km) sampling rate.

The L3 DUACS Experimental products have been developed with the aim of providing users with simple and homogeneous products along the tracks of the different altimeters, at a resolution consistent with the observable physical signal.

https://doi.org/10.5194/essd-2022-292
Preprint. Discussion started: 29 September 2022

1.2. Altimeter standards

The different altimeter standards and corrections applied are given in Table 1. The L2 upstream products considered correspond to the GDR-E standards. Some processing and corrections have however been updated in order to use the state-of-the-art recommendations from the altimetry community, and innovative processes introduced to minimize the observation errors at short wavelengths.

Innovative processing for Sentinel-3 SAR and Jason LRM:

In order to improve the sea surface height (SSH) observations, the LR-RMC (Boy et al., 2017; Moreau et al., 2021) and Adaptive (Poisson et al., 2018; Thibaut et al., 2017) processes have been used respectively for S3A, J3 and Jason-2 (J2) measurements.

The LR-RMC method is an experimental process developed by CNES. It is quite close to the current SAR processor. However, it combines the beams produced in a radar cycle differently in order to enlarge the effective footprint of the measurement and average out the effects of the sea-surface state, especially wind waves and swells that are known to impact SAR-mode performance at the short mesoscale (< ~50km). Consequently, the red noise usually observed in the spectrum of SAR sea level anomalies at short wavelength (Rieu et al, 2020) is reduced, as is the measurement noise level. This is illustrated in Figure 1. The gray spectrum corresponds to the SAR processor. It has a slightly negative slope, or “red” noise, at short wavelengths (< ~50km). Part of this error signal is assumed to be correlated with swell conditions as demonstrated by (Rieu et al., 2021). The red spectrum was generated using the LR-RMC process. In this case, the result obtained is closer to the theoretical spectrum expected, with the noise plateau visible at short wavelengths and the signal’s spectral slope visible at higher wavelengths. A direct impact of this LR-RMC processing is thus to reduce the errors at short wavelengths and allow us to better observe the short mesoscale signal of interest.

The Adaptive method is a new retracking algorithm that combines the benefits of 4 different improvements with respect to the classical MLE-4 (Maximum Likelihood Estimator) retracking algorithm currently used for the official products (Amarouche et al., 2004; Thibaut et al., 2010). First, a parameter correlated with the mean square slope of the reflective surface (MSS) has been introduced in the model. Its impact is mostly visible in the trailing edge of the echo model and allows a better fit to all types of echoes, from diffuse ones (acquired over the ocean) to very peaky echoes observed over specular regions such as leads in the Arctic Ocean, or calm lakes and rivers. Second, it directly accounts for the real in-flight Point Target Response of the instrument, by numerically convolving its discretized values to the analytical model (Poisson et al., 2018). Third, a true Maximum Likelihood Estimation method is used which accounts for the statistics of the speckle noise that corrupts the radar echo. Note that the current method implemented in the official products (up to GDR-E version) is a simple Least Square Estimation. The chosen estimation method implemented in the Adaptive solution is a geometrical method called the Nelder-Mead algorithm. Finally, the algorithm adapts the width of the window on which the fitting procedure is applied in order to remove spurious reflections coming from off nadir directions, in particular when the satellite is approaching the coastlines. The many advantages brought by the Adaptive algorithms are described by (Thibaut et al., 2021, 2017; Tourain et al., 2021). In particular, a reduction of the SSH noise level of about 10% is observed.

High Frequency Adjustment (HFA) and Sea State Bias (SSB) correction for measurement noise reduction:

The altimeter measurement is contaminated by measurement noise that limits the observability of the mesoscale at wavelengths shorter than about 100 km (Dibarboure et al., 2014; Dufau et al., 2016; Xu and Fu, 2012). For

https://doi.org/10.5194/essd-2022-292
Preprint. Discussion started: 29 September 2022

LRM measurements, the spectral hump, visible on the 20Hz spectrum at wavelengths ranging from about 10 to 50 km, contains specific noises induced by sea surface roughness heterogeneities within the 1-3 km diameter altimeter footprint (Dibarboure et al., 2014).

Another significant source of noise comes from correlations between significant wave height (SWH) and range errors that are inherent to any waveform retracking algorithm (Quartly et al., 2019; Sandwell and Smith, 2005). These correlations are used to define an HFA correction able to significantly reduce the noise on the SLA signal. The methodology used is described by (Tran et al., 2021). It was applied to all the measurements of the different LRM missions, taking into account the specific processing previously described (e.g. Adaptive retracking on Jason).

The SSB correction also allows us to reduce the effects of the presence of ocean waves at the surface. A refined 2D SSB solution was used. It was adapted to the selected retracking algorithm data and based on the standard input parameters (SWH and wind speed). The methodology is described by (Tran et al., 2021). This SSB solution also contributes to the measurement noise reduction.

This is illustrated in Figure 1 (right), which shows the J3 SLA spectral content when applying different processing. The gray spectrum corresponds to the conventional MLE4 processing. The blue spectrum was generated from measurements processed with the Adaptive processor combined with the refined 2D SSB solution. It shows a reduction in noise of about 17% compared to the conventional MLE4 processing, as mainly visible at short wavelengths (< ~50km). Note that two thirds of this reduction is induced by the adaptive processing as discussed before while one third of the reduction, i.e. about 6%, can be explained by the improved SSB solution. When applying the HFA correction (red spectrum), the energy level is reduced by about additional 26% at short wavelengths. This includes a measurement noise reduction as well as part of the spatially correlated noise visible on the LRM spectral hump (Dibarboure et al., 2014).

Up-to-date tide corrections:

Replacing the DT-2018 standards (Taburet et al., 2019) used in the conventional 1Hz DUACS product, different tide corrections have been used following the more up-to-date OSTST recommendations. A large part of these new solutions also corresponds to the standards that are used in the DUACS DT-2021 1Hz reprocessing that have been disseminated by CMEMS since the end of 2021.

The ocean tide correction used in this product was generated with the FES2014b model (Carrere et al., 2016), including the FES2014 tidal load solution.

The internal tide baroclinic signal is removed from the altimeter measurement using the Zaron (2019) (HRET 7.0) model solution. It allows the estimation of the coherent part of 4 tidal nodes (M2, K1, O1, S2). This model is defined in deep water and for medium latitudes; elsewhere, no correction is applied.

The polar tide correction is made with the Desay (2015) model taking into account the mean pole location (MPL) corresponding to the 2017 standard, including the mass loss induced by polar ice melt and recommended by IERS. Compared to the MPL 2015 standard used in the DUACS DT-2018 1Hz product, this change induces large scale sea level regional biases with a quadrupole structure of about ±1.5 cm amplitude over a short period.

Mean Sea Surface model:

The MSS model used for the SLA computation is the CNES_CLS15 model. It is referenced to the 20 year [1993, 2012] reference period. This MSS model reduces errors along the repeat tracks that are used for its computation (here J2 and J3 repeat tracks; Pujol et al, 2016). However, errors are higher at Topex/Jason and ERS/Envisat intertracks, where only a few geodetic measurements were used for the MSS estimation. As this could be a significant limitation for the observability of the short mesoscale signal (< 100km), especially with S3A

https://doi.org/10.5194/essd-2022-292
Preprint. Discussion started: 29 September 2022

measurements that were specifically processed to better resolve the small mesoscale signal, we used for this mission a specific MSS estimated along the tracks of the altimeter, named the Hybrid Mean Profile (HPM). The methodology used for the S3A HMP estimation is similar to the one described by (Dibarboure and Pujol, 2021). It includes a specific ocean variability correction to force the 20-year period the HMP should refer to, notwithstanding the limited temporal coverage of the available S3A measurements. The main differences consist of the longer temporal period considered - nearly 2.5 years - and the use of up to date altimeter standards and corrections as described in Table 1. The quality of the S3A HMP was analyzed at short wavelengths using the methodology described by (Dibarboure and Pujol, 2021). It has a mean error of 0.12 cm², i.e. about 10% of the noise-free SLA signal variance. Compared to the CNES_CLS15 reference MSS, the errors are significantly reduced, by about 70%. The main reduction in error occurs in the geodetic structures as previously observed by (Dibarboure and Pujol, 2021).

The HMP content is illustrated in Figure 2, which shows the differences between the CNES_CLS15 gridded MSS model and the S3A HMP when S3A flew over a small seamount, underlined by the bathymetric contour lines (black lines). The positive anomalies in the HPM-MSS differences correspond to additional signal in the HMP not present in the gridded reference MSS. Here the HPM-MSS differences highlight the signature of the bathymetric structure, which is flattened in the gridded reference MSS and more clearly represented in the HMP. The good consistency of the signal observed along both the S3A tracks crossing the structure allows us to have confidence in the representation of this additional signal observed in the HMP. We also note that the seamount signature on the HMP shows up at short wavelengths. The positive values crossing the seamount cover a section about 15-20 km long. This means that such a structure is difficult to accurately capture with 1Hz altimeter measurements at a sampling rate close to the Nyquist frequency. This also underscores the value in processing the altimeter measurements at a high resolution for a more accurate MSS estimation.

1.3. Valid data selection

The valid data selection criteria usually applied for the 1Hz data processor (Roinard and Michaud, 2019) use parameters that are specific to the 1Hz products and cannot be applied to the 20Hz data. Consequently, the valid data selection strategy used for the L3 5Hz production was reviewed as follows:

As for the 1Hz processing, the first step is to eliminate all measurements over land. The land-sea flag given in the L2 product is used for this purpose. Ice contaminated measurement are rejected using criteria described below. Then, basic threshold criteria on SLA and SWH are used to reject aberrant measurements. Finally, a specific analysis along each altimeter track allows us to reject invalid SLA measurements over the ocean as described below.

Ice contaminated data detection:

When available in the upstream L2 products, the waveform classification was used to reject ice contaminated measurements. This criterion was combined with the ice concentration given by OSISAF (Lavergne et al., 2019) in order to avoid measurement rejection over open water (ice concentration equal to 0%) and to apply a restrictive selection in high ice concentration areas (ice concentration > 50%). The measurements in the medium ice concentration areas (ice concentration <=50%) are rejected when the waveform corresponds to a peaky measurement, a sign of potential contamination. This specific data selection criterion was applied on S3A and AltiKa measurements.

https://doi.org/10.5194/essd-2022-292
Preprint. Discussion started: 29 September 2022

For the J2 and J3 measurements, no waveform classification was available, so only the product's ice flag was used.

For the C2 mission, neither the product ice flag nor the waveform classification were available. Instead, the OSISAF ice concentration was used with a the 50% ice concentration threshold criterion.

Open ocean data selection:

The valid data selection in the open ocean is based on an iterative kσ editing applied to the SLA and is divided into two steps. At each step, the k coefficient is optimized in order to detect as many invalid measurements as possible while maximizing the availability of valid measurements. The process is applied to each track individually. First, SLA data outliers are rejected according to a $k_1\sigma$ criterion, σ being the SLA variability along the track considered and k_1 depending on the statistical ocean variability at the location considered in order to relax the threshold criterion in high variability areas (e.g. the Gulf Stream). This avoids a too severe data rejection in high variability areas where intense mesoscale structures could otherwise be rejected. Then, the track considered is iteratively processed in order to reject invalid SLA measurements using a k_2 σ criterion applied to the short-wavelength SLA signal dominated by measurement noise. The short wavelength content of the SLA is extracted using a Lanczos filter, σ is estimated at each iteration and k_2 depends on the SWH signal using the nearly linear relationship observed between the short wavelength SLA content (dominated by measurement noise) and the SWH for SWH higher than ~2m. For lower SWH values, k_2 is set to the minimal value of 3. This avoids a too severe rejection of the SLA measurements in high SWH areas, where the noise measurement is usually higher.

1.4. Short wavelengths noise filtering and signal subsampling

In spite of the different processing and corrections applied, aiming to resolve as much as possible of the short wavelength signal, the measurement remains significantly contaminated by residual noise. A specific spectral analysis was applied in order to define the observable wavelength for the different missions. The methodology and results are discussed in more detail in section 2.1. The observable wavelengths were defined in a conservative way, considering the balanced (geostrophic) motion and noise signals. They are presented in Table 2.. They range between 35 and 55km in the North Atlantic Area, depending on the mission considered. These values are representative of each mission's measurement accuracy, and are used as cut-off wavelengths for the low-pass Lanczos filters applied to the signals. This strategy differs from the conventional DUACS 1Hz processing for which a unique, mean cut-off wavelength is used to low-pass filter the measurements, whatever the mission.

The measurements are then subsampled in order to be consistent with the observing capabilities. A final 5Hz sampling, i.e. slightly more than 1km between two consecutive measurements, was retained as a good compromise between the sampling needs and observing capabilities.

1.5. Long-Wavelength Error correction

The LWE correction is the final step for the homogenization of the multi-mission signal. Its purpose is to reduce the regional discrepancies observed between neighboring altimeter tracks. These biases are induced by, among other things, residual orbit and geophysical or environmental correction errors. For both DUACS 1Hz and 5Hz processing, the LWE is estimated by a two-step procedure: 1) A sparse estimation of the LWE correction along

https://doi.org/10.5194/essd-2022-292
Preprint. Discussion started: 29 September 2022

the track is made by Optimal Interpolation (OI); and 2) this sparse estimation is interpolated at each along-track measurement location.

There are nonetheless some differences in how the procedure is implemented for 5Hz data. First, for step 1, the sparse estimation of the LWE correction along the tracks of the altimeters is done using a 100 km sampling rate instead of the 500 km usually used in the DUACS 1Hz processing. Then for the step 2, an OI method is used to interpolate the LWE correction on each individual 5Hz measurement location, whereas the 1Hz processor uses cubic spline adjustment as described by (Le Traon et al., 1998). This OI approach allows us to finely tune the cut-off wavelength that needs to be estimated for the LWE signal, typically of the order of 2000km. Additionally, so as to account for the different dynamics of semi-enclosed seas, the different passes are split into independent segments when overflying land. This improves the LWE correction and its ability to correct the residual errors caused by a reduced quality of the various geophysical, atmospheric and environmental corrections.

An example is given in Figure 3. It shows the mean LWE correction computed for C2 1Hz measurements over year 2014, comparing the DUACS 1Hz processing (left) and the updated methodology defined for the 5Hz processing (right). When applying the DUACS 1Hz LWE processor the correction obtained does not show any specific geographical pattern that can be correlated with a physical signal. On the other hand, the LWE correction obtained applying the processor defined for the 5Hz production shows a more structured signal, with positive and negative values (up to ±1cm) aligned along the magnetic equator. This pattern evokes an ionosphere-related signal, highlighting the imprecision of the Global Ionospheric Model correction for this mission due to the lack of dual-frequency altimeter measurements.

We used statistics at cross-overs in order to quantify the impact of the LWE correction applied. Indeed, as the LWE correction acts to reduce residual long wavelength biases observed between neighboring tracks, it also reduces the variance of the SLA differences at cross-overs. Table 3 shows the mean variance of SSH differences at cross-overs for the global ocean over a one-year period , for J3. Mono-mission (J3/J3) and multi-mission (J3/Sentinel-3B (S3B)) cross-overs are considered. Here only J3 is corrected for the LWE while S3B is not used for the LWE estimation and thus remains independent. Statistics obtained when not applying the LWE correction, when applying the LWE correction deduced from the conventional DUACS 1Hz processing, and from the 5Hz processing are given. They show that the LWE correction obtained with the Duacs 1Hz processing significantly improves the consistency of the SLA between tracks and removes discrepancies at cross-overs, with a 1.5 to 2 cm² reduction in variance. The results are further enhanced when using the LWE method defined for the 5Hz processor with an additional 1 to 2.5 cm² reduction in variance, i.e. an additional improvement of 9 to 15%, respectively for multi-mission and mono-mission cross-overs, compared to the previous LWE version. The improvement is higher at mono-mission cross-overs when both the tracks are corrected (while only J3 tracks are corrected at multi-mission cross-overs).

1.6. Across-track current estimation

The geostrophic velocities in the across-track direction were estimated using a centered difference method, using 2 measurements on either side of the point considered.

https://doi.org/10.5194/essd-2022-292
Preprint. Discussion started: 29 September 2022

2. Data validation

Although 5 different altimeter missions have been processed, the validation of the product mainly focuses on the S3A and J3 missions. Indeed, the former is representative of the SAR technology while the latter is representative of the LRM measurement. Moreover, significant evolutions have been implemented on these two missions, as discussed in section 1.

The data were assessed in terms of data availability, spectral content and consistency with independent tide gauge measurements. They were also compared to the 1Hz product available on CMEMS (produced in accordance with the DUACS DT-2018 standards).

2.1. Data availability and gain brought by the 5Hz altimeter processing near the coast

The processing used for the valid data selection can have a significant impact on the data availability rate. In the L3 5Hz processing, the data selection strategy aims to optimize the rejection of the measurements retained as invalid without much reducing the data availability rate (see section 1.3). An example of the rate of rejected measurements obtained is illustrated in Figure 4 (left), for the SAR mission (S3A) and the LRM mission (J3) for January-April 2018.

For both missions, the most drastic rejection occurs in the ice-contaminated areas; Indeed, the processing applied mainly focuses on the open ocean and is not adapted to the possible measurements available over leads. As described by (Prandi et al., 2021), the observation of the SSH in such narrow ice-free areas requires a specific delay doppler processing not implemented here. Consequently, no efforts have been made to keep the measurements over leads.

Within a band extending from 5 to 10 km from the coast, there is a high rate of data rejection of more than 30%; this increases to over 60% within 5 km from the coast. In the open ocean, the rejection rate drops to between approximately 0.5 and 1% of the measurements available. We observe here that the rejection rate remains quite homogeneous in the open ocean. This is noteworthy: in the region depicted and for this season, the SSH measurements are sensitive to high SWH (see for example Roinard et al, 2020), but the optimized data selection strategy used in the full-rate processing takes into account the higher measurement noise in these areas, reducing the rejection rate in areas of high SWH (see section 2.3).

Although they are not directly comparable due to the different sampling rates, we nevertheless observe that the valid data availability in this experimental product is overall higher than for the conventional 1Hz product, especially in coastal areas, notwithstanding the high rejection rates there. The Table 5 shows statistics of the mean distance of the nearest point to the coast for which the sampling rate reaches at least 80% of the maximum number of cycles defined for the period between mid-2016 to the end of 2018. All tracks' extremities are considered over the European coasts. They show that, in the mean, the conventional 1Hz product is defined up to 10 km to the coast for the SAR mission S3A and 11km for the LRM mission J3, when this distance is nearly half as long for the 5Hz product with respectively about 5 and 6 km.

In order to assess the pertinence of the measurements retrieved near the coast, we analyzed the SLA variance when approaching the coast. Figure 5 shows the evolution of the mean SLA variance over the Norther Spanish coast as a function of the distance from the coast for J3 and S3. Only measurements with a minimal availability rate of 80% across the whole time series are considered. Statistics are computed using 2km wide bands of distance from the coast. The restricted coastal area was selected for its nearly uniform ocean dynamics, and thus avoids mixing different dynamic regimes.

https://doi.org/10.5194/essd-2022-292
Preprint. Discussion started: 29 September 2022

We first note that, especially for the J3 mission, the data availability near and even far from the coast is degraded when using the 1Hz product. This explains the discontinuities in the statistical plots for the 1Hz product. The reduced availability of the 1Hz product is caused by the more severe data selection criteria applied as discussed before. The lower sampling rate is also a factor, since with a distance of nearly 7km between consecutive measurements, and with a restricted number off passes in this area (5 passes), there is a lower likelihood of filling all the coastal distance bins. We also see that for both J3 and S3A, the SLA variance level is slightly higher for the 5Hz product than the 1Hz. For J3, it reaches 15.3 cm² for the 1Hz and 16.3 cm² for the 5Hz product. For S3A, is reaches 14.7 cm² for the 1Hz and 17.9 cm² for the 5Hz product. This is explained by the different cut-off wavelengths used for the signal filtering, ranging from 35km for S3A to 55 km for J3 at 5Hz (see section 1.4), and 65km at 1Hz. We note however that the difference remains quite low when considering the different noise levels in the upstream products used (i.e. noise variance is reduced by a factor of 20 in the 1Hz upstream product compared to the 1Hz due to the 1Hz compression). This result is made possible by the innovative processing applied for these two missions (see section 1.2) significantly reducing the noise level for the20Hz measurements.

The evolution of the SLA variance is quite stable down to nearly 30 km from the coast for both missions at both resolutions. Then it starts to increase when approaching the coast. The increase is regular and homogeneous for J3, both at 1Hz and 5Hz sampling rates. While no measurements are available for the 1Hz product within 12km of the coast, for the 5Hz product the SLA variance continues to increase at the same rate as the signal observed further offshore. The variance reaches nearly 30 cm² near the coast. For the S3A mission, the 1Hz product also reveals a nearly linear increase in SLA variance when approaching the coast. This product does not allow an accurate sampling of the signal within 5km of the coast and there is a suspicious peak of SLA variance at around 10km from the coast. This peak is not seen in the 5Hz product. The latter rather features a nearly linear increase in SLA variance down to ~5km from the coast, consistent with what was observed with the J3 mission. In the last five kilometers, the SLA variance increases sharply to reach nearly 50cm² close to the coast.

The evolution of the SLA variance suggests that the quality of the retrieved signal is better with the 5Hz product, especially within ~12km of the coast where the there is no 1Hz data. However, while various physical signals can contribute to a higher variance in the coastal area (wind-waves, trapped waves, currents, etc.), the sharp increase in variance observed with S3A in the last five kilometers rather suggests residual errors, meaning that the 5Hz products should be used with care when considering the data within ~5km of the coast.

2.2. Observing capability

The SLA Power Spectral Density (PSD) analysis was used to define the minimum wavelength associated with the dynamical structures that altimetry would be able to observe with a signal-to-noise ratio (SNR) greater than 1. The methodology applied was derived from (Dufau et al., 2016) and consists of finding the wavelength for which the SNR is equal to 1, the signal being defined by the mesoscale spectral slope and the noise by a constant value fitted to the spectral plateau (or quite flat slope) visible at the shortest wavelengths or on the residual spectral hump when its signature is well defined. The determination of the spectral slope and noise is done by least square fitting a two-line sum model to the signal PSD. The observing capability was defined over the North East Atlantic area ([10, 35°W][30, 65°N]), in order to be representative of the area of primary interest to the CMEMS community, and allows a selection of sections of tracks long enough to obtain an accurate spectral slope estimation. The full rate measurement (20 or 40Hz) was used in order to better observe the residual noise

https://doi.org/10.5194/essd-2022-292
Preprint. Discussion started: 29 September 2022

signature. The results obtained are summarized in Table 2. They are representative of the mean value over a one-year period.

The observing capability estimated with the full rate product processed as described in section 1 ranges between 35 and 55km according to the mission. As expected, the observing capability is smaller for S3A. This capability is explained by the use of SAR technology (Raney, 1998), combined with the LR-RMC processing (Boy et al., 2017; Moreau et al., 2021) applied to this mission. C2 and ALG should be able to observe up to 40km. For C2, the presence of the SAR mode measurement in a large part of the area considered, combined with the HFA correction applied for LRM mode measurement, explain this result. The Ka band used for the AltiKa mission, which has a lower noise level than the Ku band used for other LRM missions (Verron et al., 2018), combined with the HFA noise reduction processing (Tran et al., 2021), enables it to observe the small mesoscale. Finally, the LRM Jason missions should observe wavelengths longer than 55km. The slightly degraded observing capability for these missions is caused by a higher sensitivity of the measurements to the sea surface inhomogeneities producing a well-defined spectral hump (Dibarboure et al., 2014), and thus contributing to a higher noise level in the measurements, especially during the wintertime notwithstanding the HFA correction applied.

In order to be compared with the 1Hz products' observing capability, the same methodology was applied to 1Hz measurements currently available from CMEMS and processed with the conventional DUACS system. The S3A mission, representative of SAR technology, and the J3 mission, representative of LRM technology were compared. The results are also summarized in Table 2. They show that in the North Atlantic, the conventional 1Hz sampling allows the observation of wavelengths longer than about 65 (S3A) or 85 km (J3). In other words, the full rate processing applied here reduces the observable wavelength by nearly half for the SAR mission (S3A) and by one third for LRM measurements (J3). In the case of the S3A measurements, the reduction of the observable wavelength observed here is greater than the mean reduction reported by Moreau et al. (2021) when comparing the performances of SAR vs LR-RMC full-rate processing. The authors indeed reported a reduction of nearly 1/3 of the observable wavelength with LR-RMC compared to the SAR processing. However, in the present study, we do not directly compare SAR (here in 1Hz) vs LR-RMC (here in 20Hz), but instead we are comparing the capabilities of two different product lines, thus including differences in the processing strategy, i.e. differences in the retracking mode as in Moreau et al. (2021) , and also differences in the corrections and data selection. In this case, the performance of the full rate measurement is strongly linked to the area considered and cannot be extrapolated as a global mean performance. Indeed, the presence of high SWH in the North Atlantic region considered significantly increases the noise in the processed SAR and MLE4 measurements and thus reduces their observing capability. In the case of the 20Hz measurement, this effect is counterbalanced by the different processing discussed above (i.e. LR-RMC and adaptive + HFA processing).

Although the wavelengths presented in Table 2 have been used as cut-off wavelengths for low-pass filtering over the whole North Atlantic area (see section 1.4), they are not fully representative of the observing capability over the different sub-regions and seasons. Over enclosed seas, the reduced SWH resulting in lower noise levels, combined with the smaller mesoscale signal usually observed in such regions, should improve the observing capabilities for the different altimeters. An SNR equal to one has been estimated over the Black Sea region for SAR missions (S3A and C2) processed for a specific ESA project (EO4SIBS (Grégoire et al., 2022)). The results suggest that these measurements should enhance the observability of wavelengths up to about 25 to 30km in this area (not shown). In the same way, seasonal modulations of the mesoscale activity, mainly driven by the seasonal variations of the mixed layer depth (Sasaki et al., 2014), reduce the mesoscale spectral slope in winter.

https://doi.org/10.5194/essd-2022-292
Preprint. Discussion started: 29 September 2022

At the same time, higher SWH and higher sea surface inhomogeneity contribute to increase the residual noise level. As a consequence, seasonal variability of the observing capability can be observed, as previously reported by (Dufau et al., 2016) and (Vergara et al., 2019).

2.3. New insight into the altimeter spectral content with Sentinel-3A

In recent years, high resolution models combined with in situ measurements have given us new insights into ocean dynamics at short wavelengths. Several studies (Qiu et al., 2018; Rocha et al., 2016; Sasaki et al., 2014) have underlined the importance of the unbalanced motions that contribute to the energy cascade and dissipation at these wavelengths (Rocha et al., 2016; McWilliams, 2016). Combined with the balanced motions, they thus significantly contribute to the shape of the kinetic energy spectrum and the SSH spectral slope at wavelengths lower than ~150 to than 50km or less, depending on the area and the season (Qiu et al, 2018). While only a few years ago the high noise level in altimeter measurements forbade us from being able to access these wavelengths, progress in altimeter measurement now leads us to revisit the analysis of the SLA spectral content. Additionally, recent work from (Vergara et al., 2019, 2022) proposed a refined methodology for a more accurate SLA PSD analysis. Here we adapt the methodology to analyze the spectral content of the S3A measurements. Indeed, the low noise level of the SAR measurements and LR-RMC processing makes S3A the best candidate to explore the sea surface dynamics at short wavelengths.

As before, the full rate (20Hz) measurements are used in order to access the full spectral content. Although LR-RMC processing significantly reduces the measurement errors linked to swell (Moreau et al, 2021), only measurements associated with low SWH (below 4m) have been considered in order to avoid possible contamination of the signal with residual errors. The SLA PDS has been analyzed over two different areas: the Gulf Stream core, and a less energetic area located further east in the Atlantic Ocean (precise coordinates are given in Table 6). The mean SLA PDS over the years 2017 and 2018 and for the winter (February-March-April, FMA) and summer (August-September-October, ASO) seasons have been analyzed. The spectral decomposition used is similar to the one proposed by (Vergara et al., 2022) It consists of first estimating the noise level - represented by the flat signal at the shorter wavelengths (< 10 km) - then the slope characterizing the geostrophic or mesoscale signal - usually well defined at wavelengths > ~150km - and a second slope expected to be representative of the umbalanced motion visible at the small-mesoscale. Mesoscale and small-mesoscale slopes are fitted on the noise-corrected PDS using a two-line sum model. The results obtained are presented in Figure 6 and show the mean PSDs for the regions and seasons considered. The black line represents the true PSD deduced from the altimeter measurements. The 95% confidence interval is represented by the light grey band centered on the true PSD. The 3 slopes deduced from the spectral decomposition are shown as dashed red lines. The thick red line shows the theoretical spectrum deduced from the sum of the 3 different slopes. Finally, the transition scale (Lt) defined for where the mesoscale (balanced motion) to small-mesoscale (unbalanced motion) signal ratio is equal to one, is represented by the blue star. Details of the characteristics of the different PSDs are given in Table 6.

The results obtained regarding the geostrophic dynamics are consistent with those reported by previous studies (Vergara et al., 2019) . They feature dynamics close to QG theory (spectral slope close to K^{-5},(Xu and Fu, 2012) in the Gulf Stream. The spectral slope is reduced and rather close to the SQG theory in the North East Atlantic area, especially in winter (spectral slope close to $K^{-11/3}$). The seasonal variability is quite well pronounced in this latter area, with a net deepening of the slope in summer ($K^{-4.7}$) linked to the less intense mesoscale activity at

https://doi.org/10.5194/essd-2022-292
Preprint. Discussion started: 29 September 2022

short wavelength in this season, which in turn is connected to the characteristics of a shallower Mixed Layer Depth (MLD).

The slope observed at the small-mesoscale is quite flat in comparison with the one representative of the balanced motion. It indeed ranges between $K^{-1.32}$ and $K^{-1.64}$ according to the region and season considered. These values are in accordance with unbalanced motion or Internal Gravity Wave (IGW) dynamics that are expected to have an SLA PSD slope close to K^{-2} theory (Garrett and Munk, 1975). Finally, the transition between balanced and unbalanced motion is found to range between ~50 and 120 km. A mean Lt of about 53 km is observed over the Gulf Stream core, with relatively low seasonal variability (55 km in winter and 59 km in summer). On the contrary, Lt observed in the North East Atlantic domain is strongly seasonally variable with minimal values around 75km reached during the winter period and maximal value around 120 km reached during the summer period. Although the estimation error of the Lt remains quite high (up to 56km in summer in the North-East Atlantic), the results obtained are coherent with the unbalanced motion that is enhanced by a shallow MLD and strong pycnocline observed in summer (Rocha et al., 2016). The results obtained in characterizing the unbalanced motion are also consistent with those reported by (Qiu et al., 2018). The authors used a numerical model to estimate the Lt wavelength. They reported values of about 50 km in the Gulf stream, slightly more in the North East Atlantic with significant seasonal variability. The analysis of the results over the single-year seasons also suggests interannual variability in the balance between balanced and unbalanced motions. The greatest variations were observed during the winter months for the North-East Atlantic box. In this region the signature for unbalanced motion is well defined for winter 2017. Over this period, it dominates over the geostrophic and noise signals at wavelengths ranging between about 70 and 30km. However, during winter 2018 balanced motion seems to dominate the signal up to wavelengths of about 50km. In this case, the residual measurement noise does not allow us to extract the signature of the unbalanced motion for this domain/period (no shown).

The variability explained by the unbalanced motion remains however quite low, especially in the Gulf Stream or during the winter period. In that case it dominates the noise and mesoscale signals over a short 20 to 30 km wavelength band (see Figure 6a for instance). In these conditions, the observability of this signal remains limited when considering measurements that have not been optimally processed to reduce the errors at short wavelengths. This is the case with conventional SAR measurements. Indeed, with higher level, red colored noise, affecting the signal at wavelengths up to ~50km (as visible for instance in Figure 1 over the global ocean), the SAR measurement errors mask most of the unbalanced motion in areas and seasons where this component is quite low. Elsewhere, SAR measurement capabilities still allow us to resolve part of the unbalanced motion. In this way, the high-resolution SAR measurements were used to estimate the SLA spectral content over the North-East Atlantic area during the 2017 summer period. The corrections applied to the SAR measurements are consistent with those used in the LR-RMC processing described in section 1. Results obtained with SAR or LR-RMC processed measurements can be seen in Figure 7. Both the processing show nearly similar results in the Lt estimation, with 137 km obtained with LR-RMC and 132 km with the SAR. However, the sub-mesoscale spectral slope estimated with SAR remains flatter ($K^{-1.32}$) than the one deduced from LR-RMC ($K^{-1.54}$). The latter is closest to the theoretically expected K^{-2} slope (Garrett and Munk, 1975). It is clearly apparent in Figure 7 that the red noise affecting the SAR measurements dominates the signal at wavelengths shorter than 50km, when the lower level of noise achieved with the LR-RMC processing allows us to resolve the signal up to about 30km (SNR=1 considered). This leads to the lower accuracy of the unbalanced motion observation with the SAR processing. In the same way, the high-resolution measurements, optimally processed to reduce errors at short

https://doi.org/10.5194/essd-2022-292
Preprint. Discussion started: 29 September 2022

wavelengths, add a higher precision in the characterization of the unbalanced signal. Vergara et al (2022) however showed that part of this signal can be recovered with conventional 1Hz measurements. In this case, a long temporal period is used in order to reduce the errors during the estimation.

2.4. Consistency with TG

The dense tide gauge (TG) network provided by the Copernicus Marine Service (CMEMS) over European waters was used to assess the quality of the altimeter measurements. The methodology used is derived from the one described in Sánchez-Román et al (2020) and can be summarized as follow: first, TG series with anomalous events, or with significantly higher variance (more than 20 cm^2) than the altimeter data are rejected. Then, selected TG series are processed in order to obtain an SSH signal comparable with the altimeter measurement content: the tidal signal is removed using a harmonic decomposition proposed by Codiga (2011); the dynamical atmospheric signal (Carrère and Lyard, 2003), also corrected for in altimeter measurements, is removed from the TG signal. To do so, theTG series are first converted into 6-hourly records; vertical motions linked to the post-glacial rebound are also removed from the TG signal using the Peltier model (Peltier, 2004, 1998). After that, TGs and altimeter measurements are collocated using the maximal correlation score within a 25 km area around the TG stations. Note that this distance is reduced compared to the one used in (Sánchez-Román et al., 2020) (i.e. ~100 km) in order to better focus on near-coast measurements. The next step consists of rejecting time series less than 10 months long to guarantee statistical significance. Finally, global mean statistics are computed. With the aim of reconciling the different spatial sampling capabilities between the TG network and the altimetry, different weights were used for the different TG stations selected. The weights depend on the number of neighboring TGs (a maximal distance criterion of ~100km was used) that are compared with an altimeter measurement and aligned along the same altimeter ground track. This processing was applied to S3A and J3 1Hz and 5Hz products. A filtered SLA signal, as disseminated in both 1Hz and 5Hz altimeter products, was used. The results are compared for TG stations that are common to both altimeter products. The data were compared over the period from July 2016 to September 2018.

The results obtained for S3A and J3 are quite consistent. They are presented in Figure 8, which shows the variance of the differences between altimetry and TG signals when using the 5Hz altimetry product for S3A and J3 (top), as well as the differences with the results obtained when using 1Hz altimeter products over the common TG stations selected (bottom). Results are expressed as percentages of the TG signal.

The TG selection criteria allowed us to select 232 TG sites for the comparison with S3A and 99 sites with J3 5Hz altimeter products i.e. respectively ~63 and 27 % of the initial number of the TG available. They are located along the main part of the European coasts, except in the Black Sea and West Mediterranean Sea. The mean distance between the TGs and the altimeter measurements selected is around 20km for both of the altimeter missions. The variance of the differences between the altimeter and the TG measurements shows a spatial distribution close to the observation reported by (Sánchez-Román et al., 2020) when using CMEMS 1Hz altimeter products, except that values observed here are slightly higher due to the restricted area used for the altimetry and TG measurement colocation as discussed before. The lower variances (globally < ~15%) are located in the Baltic Sea, while higher values (> 50%) are located in the Northern West Shelves area.

The number of TG stations retained as statistically comparable with the altimeter measurements is higher for the 5Hz product. Indeed, an additional 75 stations are selected with the 5Hz S3A product, i.e. ~+48% compared to the number of stations selected when using the 1Hz altimeter product. For J3, additional 30 stations are selected

https://doi.org/10.5194/essd-2022-292
Preprint. Discussion started: 29 September 2022

(i.e. +43%). They are mainly located in the Northern Sea, Gulf of Finland, in the Baltic Sea or in the jagged western UK coasts (not shown). This is due to the higher availability of 5Hz measurements in coastal areas as discussed in section 2.1.

Finally, only 142 and 62 TGs stations have been used to compare the respective performances of the S3A and J3 5Hz and 1Hz altimeter products. They correspond to the common TG stations selected for both products. The mean statistics observed for the common TG stations are given in Table 7 and Table 8, while the Figure 8 (bottom) shows the reduction of the variance of the difference between altimetry and the TG signal when using a 5Hz altimeter product rather than a 1Hz product. The results show that the mean distance between the TG and the altimeter's most correlated point for 1Hz and 5Hz altimeter products is nearly the same (~20km). Nevertheless, the length of the altimeter/TG data pair series is generally longer for the 5Hz altimeter product, with 8.7% additional pairs for S3A and 5.7% for J3, compared to the results obtained with 1Hz altimeter measurements. Here again, this is due to the enhanced data availability of the 5Hz product near the coast. We also observe in Table 7 and Table 8 that the altimeter signal retrieved with the 5Hz product is overall more consistent with the TG signal. Indeed, the 5Hz SLA shows a mean variance of the signal (126 cm² for S3A; 131 cm² for J3) quite close to the mean variance of the TG signal (134 and 154 cm² respectively). The mean variance of the differences between altimeter and TG signal reaches 58 cm² for S3A and J3 i.e. between ~43% (S3A) and 38% (J3) of the TG signal. It is reduced by about 17% for J3 to 5% for S3A when compared to the results obtained with altimeter 1Hz product. This reduction is however not homogeneous in space (Figure 8). It shows quite well-defined areas where the 5Hz altimeter product better compares with TG measurements. This is the case for instance along the West and South Iberian coasts or along the Italian coasts. On the other hand, 1Hz product for S3A performs better along the Ligurian coast or the North Iberian coast. Along the Northern European coasts, the 5Hz product is closer to the TG signal in most TG locations. However neighboring TG locations can have very different results especially along jagged coasts.

3. Use cases

3.1. Assimilation in numerical models

The 5Hz altimeter products have been designed to serve the CMEMS community and more specifically the Model Forecasting Centers (MFCs) that contribute to CMEMS. The experimental 5Hz product was thus proposed to different MFCs for testing, with the main objective to demonstrate the added value of a higher spatially resolved altimeter product for regional models. They used this product for assimilation in regional models in comparison with the results obtained with the assimilation of the conventional 1Hz product (CMEMS SEALEVEL_EUR_PHY_L3_REP_OBSERVATIONS_008_061 regional product line corresponding to the DUACS DT-2018 standards). In order to avoid biased results, possibly induced by the improved quality of the signal induced by the different instrumental and geophysical correction applied in the 5Hz processing (see section 1.2), an intermediate version of the experimental product was used for this exercise. It was constructed using altimeter standards quite close to the corresponding 1Hz products available in CMEMS, and of the revised processing method only the HFA correction, necessary to significantly reduce the error at short wavelengths, was applied in the L3 5Hz processing for this comparison.

An example of the results obtained with the 1/36°x1/36° Iberian and Bay of Biscay (IBI) model is fully described by (Benkiran et al., 2017); we summarize them here. The authors showed that the assimilation of the 5Hz SLA reduces the rms of the differences (rmse) between the model forecast and altimeter SLA along J3

https://doi.org/10.5194/essd-2022-292
Preprint. Discussion started: 29 September 2022

tracks. They report a reduction of nearly 9% of the rmse compared to the assimilation of the conventional 1Hz product. But this result can be improved when the assimilation scheme is enhanced by fully exploiting the variables delivered in the 5Hz altimeter product. Thus, using the DAC, ocean tide, internal tide and LWE corrections to adjust the altimeter content to the SSH resolved by the model, a larger reduction of the rmse can be obtained. The authors report a reduction of 11 to 14% depending on the region considered. The best scores are in areas where DAC and tide signals are significant. In the same time, the surface currents resolved by the model, when assimilating the 5Hz rather than the 1Hz altimeter measurements, are more consistent with independent observation from High Frequency Radar (Copernicus Marine In Situ Tac, 2020) with 15 to 20% reduction of the rms of the differences. There was no impact on the consistency between the model SST or T/S profiles and independent satellite or in situ observations.

3.2. Coastal currents

The experimental 5Hz L3 products can be used in studies of ocean dynamics and more particularly ocean circulation. We take here the example of the Northern Current (NC) in the western Mediterranean Sea. The J3 track #222 is well known to be optimally positioned to sample the narrow surface boundary NC flowing along the coast from Italy to Spain. At the same time, it crosses a challenging area for altimetry since it is located over a narrow and uneven shelf. This track was widely used in previous studies as for instance by (Birol et al., 2021, 2017) or (Carret et al., 2018). For comparison, the signal along the tracks S3A #513 and #741 was also considered. The track #513 is located ~0.5° west of the J3 track, just east of the La Valette island, and is optimally positioned to catch the NC over an area where the continental slope is narrow. On the contrary, the track # 741 is located east of the J3 track and crosses the NC off the Western Italian coast, around 7.9°E.

The mean geostrophic current over the year 2018, was analyzed from both 5Hz L3 altimeter products presented in this paper and a contemporaneous 1Hz product available on CMEMS (SEALEVEL_EUR_PHY_L3_REP_OBSERVATIONS_008_061 regional product line corresponding to the DUACS DT-2018 standards). In the case of the 5Hz product, the mean current was directly computed as a temporal mean of the total current, i.e. composed of the anomaly of the geostrophic current and mean absolute current both delivered in the product (i.e. mdt_velocity and sla_velocity variables). In the case of the 1Hz product, the across-track velocities are not provided. They were thus estimated using the finite difference method described in section 1.6. Then a temporal mean of the current was estimated as previously done with the 5Hz product. The MDT field used corresponds to the SMDT_MED_2014 (Rio et al., 2014) for both the 5Hz and 1Hz data processings. For both products, only measurements with a minimum rate of availability of 66% are considered.

The result is shown in Figure 9 as a function of the distance to the coast. The thick blue and red lines represent the mean current over the year deduced from respectively the 5Hz and 1Hz L3 product. The thin black lines show the variations of the current over the seasons, derived from the 5Hz product.

The figure shows that the 5Hz altimeter product perfectly captures the NC. The core current is located between ~15 and 40km from the coast along the J3 track #222 and S3A track # 741. This corresponds quite well to previous observations made with in situ measurements (Carret et al., 2018; Poulain et al., 2012). The position observed along S3A track # 513 is rather between 20 and 45km from the coast, just south of the steep bathymetric gradient observed in the area. Here again, this is consistent with previous observations (Carret et al., 2018). The intensity of the NC varies from one position to the other. For 2018, it is about 0.4 m/s in the eastern

https://doi.org/10.5194/essd-2022-292
Preprint. Discussion started: 29 September 2022

position (S3A track #741). A higher intensity, 0.6 m/s~, is observed in the Western part (S3A track # 513), while a lower intensity, about 0.3 m/s is observed along the central J3 track (#222). These observations range the values previously reported with in situ measurements. Carret et al. (2018) for instance reported a mean current intensity slightly more than 0.3 m/s observed by glider in an area just West of S3A track 741. The same authors also reported a higher current intensity (~0.44 m/s) observed with HF radar South of Toulon, corresponding to the position of S3A track #513. The acceleration of the stream in the area was also observed with high resolution numerical models (Ourmières et al., 2011). Meanwhile drifter measurements analyzed by (Poulain et al., 2012) showed a weakening of the stream in the Manton/Nice area (i.e. just eastward of the J3 pass), in correlation with the general broadening of the continental shelf and slope. The mean current intensity measured with J3 track #222 is in agreement with the one reported by (Birol et al., 2021) who studied X-TRACK/ALES 20Hz altimeter products along the same track, except that these authors analyzed the signal over a longer time period. Nevertheless, the intensity of the stream here observed with J3 could be slightly underestimated due to the higher residual noise level in these measurements and the resulting higher cut-off wavelength compared to that used for the S3A processing (see §1.4).

The results from 1Hz product also clearly show the signature of the NC current, however with a lower precision than observed with the 5Hz altimeter product. Indeed, when the 1Hz altimeter product is used, the current intensity is reduced compared to the results obtained with 5Hz product, especially along the S3A tracks (a difference of more than 0.2 m/s). Additionally, the vein of the current observed with the 1Hz product is wider than with the 5Hz product, and shifted farther from the coast, as observed along tracks #513 and 222. This is partly explained by the different spatial filtering applied to the SLA measurements, with a cut-off around 45km applied in the 1Hz processing (Taburet et al., 2019). Furthermore, as previously discussed (§2.1), the 1Hz product does not accurately capture the part of the signal located close to the coast.

Previous authors have reported a NC that is more intense, narrower and flows closer to the coast during the winter months (Alberola et al., 1995; Petrenko et al., 2008; La Violette, 1994). However, a higher barotropic instability, inducing associated mesoscale activity, is observed in the autumn and winter months and can significantly perturb the mean flow (Guihou et al., 2013; Millot, 1991; Sammari et al., 1995). The seasonal mean current obtained from the 5Hz altimeter product is shown with black lines in Figure 9. It shows high variability. Along S3A tracks #513 and #741, the seasonal variability corresponds quite well to the mean tendency, with an intense stream during the winter months (respectively up to 0.8 and 0.5 m/s in OND) and less intense during the spring and summer, (respectively ~0.5 m/s in AMJ and 0.4 m/s in JJA). Additionally, the current is shifted slightly further from the coast during this last season. We note however for track #741 that an intense stream is also observed during the months of April, May and June. This behavior differs from the mean variability reported by previous authors. During this period S3A measurements are not available over one cycle. The AMJ mean statistics are thus deduced from only 2 cycles of measurements (against 3 in nominal situation). With a 10-day temporal sampling, the seasonal variability deduced from J3 measurements are statistically more robust. However, over the year considered, the seasonal variability observed along J3 track #222 also shows anomalies with the higher intensity of the stream reached during the summer period (0.4 m/s in JAS). An intensification of the NC in the area is indeed clearly visible over 5 successive cycles in July and August, suggesting that this signal is physical and does not correspond to an anomaly of the measurement. A similar behavior was observed along the same J2 track during the 2014-2015 period as reported by (Carret et al., 2018). The authors argued that HF radar measurements, located more westward from the J2 track location, suggest that this observed NC

https://doi.org/10.5194/essd-2022-292
Preprint. Discussion started: 29 September 2022

intensification is realistic. It could correspond to the large year to year variations of the NC seasonal variability also reported by (Birol et al., 2017).

4. Data availability

The DUACS L3 5Hz experimental altimeter products (https://doi.org/10.24400/527896/a01-2021.003,(Pujol et al., 2020b); https://doi.org/10.48670/moi-00137,(Pujol et al., 2020a)) presented in this paper are available on AVISO+ (https://www.aviso.altimetry.fr/en/data/products/sea-surface-height-products/regional/ssalto/duacs-experimental-products.html) and from the CMEMS catalog (SEALEVEL_ATL_PHY_HR_L3_MY_008_064 product line; https://doi.org/10.48670/moi-00137). They cover the North Atlantic Area (Latitudes > 10°N), European Seas (Mediterranean, Black Sea and Baltic Sea) and Arctic region (Latitudes > 50°N). The data are available from mid-2016 to the end of 2018. The missions included are S3A, J3, J2 (interleaved then Long Repeat Orbit phase), SARAL-DP/AltiKa (ALG) and C2.

The data are disseminated in the NetCDF format. Each file contains 1 day of measurements for one mission. The geophysical variables provided (listed in Table 4) correspond to the SLA processed as described in section 1, different geophysical corrections applied as described in Table 1**Erreur ! Source du renvoi introuvable.** and section 1, auxiliary product used in the processing (MDT) and derived across-track geostrophic current. All the geophysical corrections discussed above have been applied on the altimeter measurement, i.e. the SLA field delivered does not contain the corresponding signals. The users can however reinject one or more of these signals in the SLA as described in Table 4 and according to their needs and applications.

5. Summary and perspectives

We presented in this paper an experimental DUACS L3 altimeter sea level product defined with a 5Hz sampling rate. This product was developed with support from CNES in preparation for the next generation of operational altimeter products that will be disseminated by CMEMS in the near future. It is intended to fulfill the specific requirements for regional applications, and in particular contribute to improving the performance of high-resolution numerical models via assimilation.

The processes applied to this product are quite similar to the ones used in the conventional DUACS 1Hz product currently available on CMEMS. However, significant improvements have been implemented at different steps of the processing, from the choice of the upstream products and corrections applied, to the final residual noise filtering, data selection strategy and multi-mission cross-calibration. They all contribute to the 5Hz product's better ability to resolve the small mesoscale signal compared to the corresponding 1Hz product.

Indeed, quality assessment first revealed an improved observability of the small-scale signal with the 5Hz product, both in open ocean and coastal areas. This is possible above all thanks to the higher sampling rate of the full rate (20Hz to 40Hz) altimeter measurements used for this product, but also the different innovative and up-to-date altimeter processing and corrections minimizing the measurement noise and permitting the resolution of the small mesoscale signal. The LR-RMC processing (Boy et al., 2017; Moreau et al., 2021) applied to S3A SAR measurements significantly reduces the red noise signal induced by wind waves and swells observed in conventional SAR processing (Rieu et al, 2020). The adaptive processing (Poisson et al., 2018; Thibaut et al., 2021) applied to Jason LRM measurements reduces noise measurement by about 10% compared to the conventional MLE4 processing (Thibaut et al., 2021) Improved SSB and HFA corrections improve on this with an additional about 30% reduction in noise (Tran et al., 2021). The data recovery strategy used for the 5Hz

https://doi.org/10.5194/essd-2022-292
Preprint. Discussion started: 29 September 2022

product also optimizes the data availability. This is especially the case over high SWH areas where, when using the full rate altimeter editing strategy, the data rejection rate remains quite similar to the one observed in low SWH areas, while a higher rejection rate is usually had with the DUACS 1Hz editing strategy. Finally, the observable mesoscale wavelengths estimated from the full-rate processed measurements is reduced by a factor of up to 1/3 to 1/2 compared to the 1Hz products in the North East Atlantic, where the presence of high SWH helps to amplify this result. Low-pass filtering, used to reduce residual signal noise on the delivered SLA, was fitted according to the observing capability of the different altimeters. The approach remains quite conservative compared to the 1Hz production since we only consider the balanced motion. Nevertheless, the L3 5Hz product allows the observation of mean wavelengths of up to ~55km for the Jason LRM mission and ~35km with the S3A SAR mission.

The signal at long-wavelengths is also improved in the 5Hz processing thanks to a more accurate estimation of the LWE correction. It reduces the SLA discrepancies at cross-over points by ~9-15% (i.e. 1 to 2.5 cm²) compared to the LWE correction that can be retrieved using the DUACS 1Hz processing.

In coastal areas, the 5Hz experimental product provides more accurate measurements in the band lying between 5 and 10km from the coast compared to the 1Hz product. Indeed, it offers good measurements up to ~5-6 km beyond which data availability for the 1Hz product is reduced, especially starting from between 10-11km from the coast. The dense European TG network was used in order to assess the data quality in coastal areas. The consistency with TG measurements is higher with the 5Hz altimeter product than with the conventional 1Hz product. This is first of all because when using the 5Hz altimeter product a higher number of TG stations are selected for comparison with altimetry (+48% for S3A, +43% for J3); secondly, the number of altimetry-TG measurement data pairs is also higher when the 5Hz product is used (+8.7% for S3A, +5.7% for J3); and thirdly, the variance of the differences between altimetry and the TG signal is also significantly reduced with the 5Hz altimeter product (-5% for S3A, -17% for J3). Further improvements with J3 are because of the higher performance of the adaptive retracking in coastal areas than with the conventional MLE4 processing. It remains to be said that LRRMC processing applied to S3A is not optimized for the coastal band even if the results obtained remain quite good.

All these improvements make the DUACS experimental 5Hz product valuable and useful for different applications. Modern numerical models with their ever-increasing resolutions, can benefit from the 5Hz altimeter product, as pointed out by Benkiran et al (2021). These authors showed that high resolution (1/36°x1/36°) numerical model analysis can be improved by optimally assimilating the 5Hz product rather than the 1Hz product (analysis rmse reduction of 9%). We also showed in this paper that the analysis of a specific coastal current in the Northern Mediterranean Sea demonstrates the 5Hz product's enhanced ability in resolving narrow current veins located close to the coast.

Additionally, the high signal to noise ratio observed with S3A allows us to resolve short wavelengths and can contribute to a better understanding of the upper ocean sea surface dynamics that include both balanced and unbalanced components. These very encouraging results were however observed over two specific areas and using favorable data selection. The small-scale content of the SAR measurements processed with LRRMC should be further analyzed to identify possible residual errors. Nevertheless, the result suggests that a larger part of the small-scale signal may be exploited. The conservative noise filtering previously applied to 5Hz L3 processing may thus evolve in a future version to better take into account the observability of unbalanced motions. We may infer that that these results will apply equally to the SWOT mission, which is expected to feature lower measurement noise as well. Indeed, the Karin noise in the center of the swath (between ~25 and 45

https://doi.org/10.5194/essd-2022-292
Preprint. Discussion started: 29 September 2022

775 km from the nadir) is expected to range between 2 and 2.5 cm rms for the same SWH selection criterion (< 4m) (Esteban Fernendez et al., 2017) used in this paper for S3A. This is less than half the noise level of the S3A measurements (i.e. between ~4 and 4.5 cm rms). The equivalent noise level should be reached with SWOT measurements for SWH ranging between 5 and 6 m. This suggests that, if properly corrected for other sources of expected errors from the swath measurement at short wavelength, SWOT should offer us an excellent
780 opportunity to resolve the unbalanced motion.

The experimental 5Hz DUACS product presented in this paper has the required qualities to serve the CMEMS and scientific communities and is a candidate for implementation in operational production. Nevertheless, other improvements are still possible, by taking advantage of the experience acquired by other projects and scientific communities and considering other advances recently made in altimeter processing. For instance, the ESA
785 EO4SIBS project (Grégoire et al., 2022), focusing on the Black Sea region, has shown that the DUACS full rate data recovery strategy can be improved with a more accurate detection of ice or land contaminated measurements at regional scale, taking advantage of different retracking parameters (e.g. peakiness). The X-TRACK processing (Birol et al., 2021, 2017) also relies on a different data recovery strategy that was demonstrated to accurately recover SSH measurements where some invalid geophysical or environmental
790 corrections would have flagged the measurement as missing. Alternative altimeter measurement processing, that more accurately retrieves the signal at short wavelengths or in specific tricky areas (e.g. ice or land contaminated) are also available (e.g. ALES (Passaro et al., 2014); FF-SAR (Egido and Smith, 2017). Innovative processing techniques are also proposed in order to drastically reduce or filter measurement noise (e.g. EMD filtering (Quilfen and Chapron, 2021)). All of these advances should be evaluated and considered for future
795 inclusion. There will also be new challenges in the future, such as improving the processing in coastal areas, especially in the 0-10km near-coast band, the recovery of the measurements over leads areas, requiring specific processes as demonstrated for instance by (Auger et al., 2022), and the possible extension of the full rate L3 altimeter processing over the global ocean.

References

800 Alberola, C., Millot, C., and Font, J.: On the seasonal and mesoscale variabilities of the Northern Current during the PRIMO-0 experiment in the western Mediterranean-sea, Oceanol. Acta, 18, 163–192, 1995.

Amarouche, L., Thibaut, P., Zanife, O. Z., Dumont, J.-P., Vincent, P., and Steunou, N.: Improving the Jason-1 Ground Retracking to Better Account for Attitude Effects, Mar. Geod., 27, 171–197, https://doi.org/10.1080/01490410490465210, 2004.

805 Auger, M., Prandi, P., and Sallée, J.-B.: Southern ocean sea level anomaly in the sea ice-covered sector from multimission satellite observations, Sci. Data, 9, 70, https://doi.org/10.1038/s41597-022-01166-z, 2022.

Benkiran, M., Remy, E., and Reffray, G.: Impact of the assimilation of high-frequency data in a regional model with high resolution, OSTST, Miami, USA, https://ostst.aviso.altimetry.fr/programs/abstracts-details.html?tx_ausyclsseminar_pi2%5BobjAbstracte%5D=2264&cHash=2f51a0cad63bed9bfca610178667ffab,
810 2017.

https://doi.org/10.5194/essd-2022-292
Preprint. Discussion started: 29 September 2022

Benveniste, J., Cazenave, A., Vignudelli, S., Fenoglio-Marc, L., Shah, R., Almar, R., Andersen, O., Birol, F., Bonnefond, P., Bouffard, J., Calafat, F., Cardellach, E., Cipollini, P., Le Cozannet, G., Dufau, C., Fernandes, M. J., Frappart, F., Garrison, J., Gommenginger, C., Han, G., Høyer, J. L., Kourafalou, V., Leuliette, E., Li, Z., Loisel, H., Madsen, K. S., Marcos, M., Melet, A., Meyssignac, B., Pascual, A., Passaro, M., Ribó, S., Scharroo, R., Song, Y. T., Speich, S., Wilkin, J., Woodworth, P., and Wöppelmann, G.: Requirements for a Coastal Hazards Observing System, Front. Mar. Sci., 6, 2019.

Birol, F., Fuller, N., Lyard, F., Cancet, M., Niño, F., Delebecque, C., Fleury, S., Toublanc, F., Melet, A., Saraceno, M., and Léger, F.: Coastal applications from nadir altimetry: Example of the X-TRACK regional products, Adv. Space Res., 59, 936–953, https://doi.org/10.1016/j.asr.2016.11.005, 2017.

Birol, F., Léger, F., Passaro, M., Cazenave, A., Niño, F., Calafat, F. M., Shaw, A., Legeais, J.-F., Gouzenes, Y., Schwatke, C., and Benveniste, J.: The X-TRACK/ALES multi-mission processing system: New advances in altimetry towards the coast, Adv. Space Res., 67, 2398–2415, https://doi.org/10.1016/j.asr.2021.01.049, 2021.

Boy, F., Moreau, T., Rieu, P., Aublanc, J., Thibaut, P., Mavrocordatos, C., Femenias, P., and Picot, N.: New stacking method for removing the SAR sensitivity to swell, OSTST, Miami, USA, https://swot.jpl.nasa.gov/system/documents/files/2176_2176_D-61923_SRD_Rev_B_20181113.pdf, 2017.

Capet, X., McWilliams, J. C., Molemaker, M. J., and Shchepetkin, A. F.: Mesoscale to Submesoscale Transition in the California Current System. Part III: Energy Balance and Flux, J. Phys. Oceanogr., 38, 2256–2269, https://doi.org/10.1175/2008JPO3810.1, 2008.

Carrère, L. and Lyard, F.: Modeling the barotropic response of the global ocean to atmospheric wind and pressure forcing - comparisons with observations, Geophys. Res. Lett., 30, https://doi.org/10.1029/2002GL016473, 2003.

Carrere, L., Lyard, F., Allain, D., Cancet, M., Picot, N., Guillot, A., Faugère, Y., Dupuy, S., and Baghi, R.: Final version of the FES2014 global ocean tidal model, which includes a new loading tide solution, OSTST, La Rochelle, France, https://ostst.aviso.altimetry.fr/fileadmin/user_upload/tx_ausyclsseminar/files/Poster_FES2014b_OSTST_2016.pdf, 2016.

Carret, A., Birol, F., Estournel, C., Zakardjian, B., and Testor, P.: Synergy between in situ and altimetry data to observe and study the NorthernCurrent variations (NW Mediterranean Sea), Remote Sensing/Current Field/All Depths/Mediterranean Sea, https://doi.org/10.5194/os-2018-76, 2018.

Cartwright, D. E. and Edden, A. C.: Corrected Tables of Tidal Harmonics, Geophys. J. Int., 33, 253–264, https://doi.org/10.1111/j.1365-246X.1973.tb03420.x, 1973.

Cartwright, D. E. and Tayler, R. J.: New Computations of the Tide-generating Potential, Geophys. J. Int., 23, 45–73, https://doi.org/10.1111/j.1365-246X.1971.tb01803.x, 1971.

Codiga, D.: Unified tidal analysis and prediction using the UTide Matlab functions, https://doi.org/10.13140/RG.2.1.3761.2008, 2011.

https://doi.org/10.5194/essd-2022-292
Preprint. Discussion started: 29 September 2022

Copernicus Marine In Situ Tac: For Global Ocean-Delayed Mode in-situ Observations of surface (drifters and HFR) and sub-surface (vessel-mounted ADCPs) water velocity. Quality Information Document (QUID), CMEMS--QUID-013-044, https://doi.org/10.13155/41256, 2020.

Cotton, D., Naeije, M., Scharroo, R., Gommenginger, C., Cipollini, P., Clarizia, M.-P., Egido, A., Garcia, P. N., Roca, M., Moreau, T., Raynal, M., Andersen, O., Stenseng, L., Cancet, M., Fernandes, M. J., and Boy, F.: CP40 - Cryosat Plus for Oceans : CP40 ESA contract No 4000106169/12/I-NB, 65, 2015.

Desai, S., Wahr, J., and Beckley, B.: Revisiting the pole tide for and from satellite altimetry, J. Geod., 89, 1233–1243, https://doi.org/10.1007/s00190-015-0848-7, 2015.

Dibarboure, G. and Pujol, M.-I.: Improving the quality of Sentinel-3A data with a hybrid mean sea surface model, and implications for Sentinel-3B and SWOT, Adv. Space Res., 68, 1116–1139, https://doi.org/10.1016/j.asr.2019.06.018, 2021.

Dibarboure, G., Pujol, M.-I., Briol, F., Traon, P. Y. L., Larnicol, G., Picot, N., Mertz, F., and Ablain, M.: Jason-2 in DUACS: Updated System Description, First Tandem Results and Impact on Processing and Products, Mar. Geod., 34, 214–241, https://doi.org/10.1080/01490419.2011.584826, 2011.

Dibarboure, G., Boy, F., Desjonqueres, J. D., Labroue, S., Lasne, Y., Picot, N., Poisson, J. C., and Thibaut, P.: Investigating Short-Wavelength Correlated Errors on Low-Resolution Mode Altimetry, J. Atmospheric Ocean. Technol., 31, 1337–1362, https://doi.org/10.1175/JTECH-D-13-00081.1, 2014.

Ducet, N., Le Traon, P. Y., and Reverdin, G.: Global high-resolution mapping of ocean circulation from TOPEX/Poseidon and ERS-1 and -2, J. Geophys. Res. Oceans, 105, 19477–19498, https://doi.org/10.1029/2000JC900063, 2000.

Dufau, C., Martin-Puig, C., and Moreno, L.: User Requirements in the Coastal Ocean for Satellite Altimetry, in: Coastal Altimetry, edited by: Vignudelli, S., Kostianoy, A. G., Cipollini, P., and Benveniste, J., Springer, Berlin, Heidelberg, 51–60, https://doi.org/10.1007/978-3-642-12796-0_3, 2011.

Dufau, C., Orsztynowicz, M., Dibarboure, G., Morrow, R., and Le Traon, P.: Mesoscale resolution capability of altimetry: Present and future, J. Geophys. Res. Oceans, 121, 4910–4927, https://doi.org/10.1002/2015JC010904, 2016.

Egido, A. and Smith, W. H. F.: Fully Focused SAR Altimetry: Theory and Applications, IEEE Trans. Geosci. Remote Sens., 55, 392–406, https://doi.org/10.1109/TGRS.2016.2607122, 2017.

Esteban Fernendez, D., Fu, L.-L., Pollard, B., Vaze, P., Abelson, R., and Steunou, N.: SWOT Project: MISSION PERFORMANCE AND ERROR BUDGET, Jet Propulsion Laboratory, https://swot.jpl.nasa.gov/system/documents/files/2178_2178_SWOT_D-79084_v10Y_FINAL_REVA__06082017.pdf, 2017.

Fernandes, M. J. and Lázaro, C.: GPD+ Wet Tropospheric Corrections for CryoSat-2 and GFO Altimetry Missions, Remote Sens., 8, 851, https://doi.org/10.3390/rs8100851, 2016.

https://doi.org/10.5194/essd-2022-292
Preprint. Discussion started: 29 September 2022

880 Ferrari, R. and Wunsch, C.: Ocean Circulation Kinetic Energy: Reservoirs, Sources, and Sinks | Annual Review of Fluid Mechanics, Annu. Rev. Fluid Mech., 41, 253–282, https://doi.org/10.1146/annurev.fluid.40.111406.102139, 2008.

Garrett, C. and Munk, W.: Space-time scales of internal waves: A progress report, J. Geophys. Res. 1896-1977, 80, 291–297, https://doi.org/10.1029/JC080i003p00291, 1975.

885 Gommenginger, C., Thibaut, P., Fenoglio-Marc, L., Quartly, G., Deng, X., Gómez-Enri, J., Challenor, P., and Gao, Y.: Retracking Altimeter Waveforms Near the Coasts, Coast. Altimetry, 61, 2010.

Grégoire, M. and EO4SIBS consortium (ESA project): Earth Observation products for Science and Innovation in the Black Sea, EGU21, Gather Online, event: EGU21DOI: 10.5194/egusphere-egu21-10237, https://meetingorganizer.copernicus.org/EGU21/EGU21-10237.html, 2021.

890 Grégoire, M., Alvera-Azcarata, A., Buga, L., Capet, A., Constantin, S., D'Ortenzio, F., Doxaran, D., Faugeras, Y., Garcia-Espriu, A., Golumbeanu, M., Gonzales-Haro, C., Gonzales-Gambau, V., Kasprzyk, J.-P., Ivanov, E., Mason, E., Mateescu, R., Meulders, C., Olmedo, E., Pons, L., Pujol, M.-I., Sarbu, G., Turiel, A., Vandenbulcke, L., and Rio, M.-H.: Monitoring Black Sea environmental changes from space, Earth Syst. Sci. Data, 2022.

Guihou, K., Marmain, J., Ourmières, Y., Molcard, A., Zakardjian, B., and Forget, P.: A case study of the
895 mesoscale dynamics in the North-Western Mediterranean Sea: a combined data–model approach, Ocean Dyn., 63, 793–808, https://doi.org/10.1007/s10236-013-0619-z, 2013.

Iijima, B. A., Harris, I. L., Ho, C. M., Lindqwister, U. J., Mannucci, A. J., Pi, X., Reyes, M. J., Sparks, L. C., and Wilson, B. D.: Automated daily process for global ionospheric total electron content maps and satellite ocean altimeter ionospheric calibration based on Global Positioning System data, J. Atmospheric Sol.-Terr. Phys., 61,
900 1205–1218, https://doi.org/10.1016/S1364-6826(99)00067-X, 1999.

Klein, P., Hua, B. L., Lapeyre, G., Capet, X., Le Gentil, S., and Sasaki, H.: Upper Ocean Turbulence from High-Resolution 3D Simulations, J. Phys. Oceanogr., 38, 1748–1763, https://doi.org/10.1175/2007JPO3773.1, 2008.

La Violette, P. E.: Seasonal and Interannual Variability of the Western Mediterranean Sea, American Geophysical Union, 372 pp., 1994.

905 Lavergne, T., Sørensen, A. M., Kern, S., Tonboe, R., Notz, D., Aaboe, S., Bell, L., Dybkjær, G., Eastwood, S., Gabarro, C., Heygster, G., Killie, M. A., Brandt Kreiner, M., Lavelle, J., Saldo, R., Sandven, S., and Pedersen, L. T.: Version 2 of the EUMETSAT OSI SAF and ESA CCI sea-ice concentration climate data records, The Cryosphere, 13, 49–78, https://doi.org/10.5194/tc-13-49-2019, 2019.

Le Traon, P. Y., Nadal, F., and Ducet, N.: An Improved Mapping Method of Multisatellite Altimeter Data, J.
910 Atmospheric Ocean. Technol., 15, 522–534, https://doi.org/10.1175/1520-0426(1998)015<0522:AIMMOM>2.0.CO;2, 1998.

Lyard, F. H., Allain, D. J., Cancet, M., Carrère, L., and Picot, N.: FES2014 global ocean tide atlas: design and performance, Ocean Sci., 17, 615–649, https://doi.org/10.5194/os-17-615-2021, 2021.

https://doi.org/10.5194/essd-2022-292
Preprint. Discussion started: 29 September 2022

McWilliams, J. C.: Submesoscale currents in the ocean, Proc. R. Soc. Math. Phys. Eng. Sci., 472, 20160117, https://doi.org/10.1098/rspa.2016.0117, 2016.

Mercator Ocean and CMEMS partners: CMEMS requirements for the evolution of the Copernicus Satellite Component, 2017.

Mercier, F., Rosmorduc, V., Carrere, L., and Thibaut, P.: Coastal and Hydrology Altimetry product (PISTACH) handbook, 2010.

Millot, C.: Mesoscale and seasonal variabilities of the circulation in the western Mediterranean, Dyn. Atmospheres Oceans, 15, 179–214, https://doi.org/10.1016/0377-0265(91)90020-G, 1991.

Moreau, T., Cadier, E., Boy, F., Aublanc, J., Rieu, P., Raynal, M., Labroue, S., Thibaut, P., Dibarboure, G., Picot, N., Phalippou, L., Demeestere, F., Borde, F., and Mavrocordatos, C.: High-performance altimeter Doppler processing for measuring sea level height under varying sea state conditions, Adv. Space Res., 67, 1870–1886, https://doi.org/10.1016/j.asr.2020.12.038, 2021.

Mulet, S., Rio, M.-H., Etienne, H., Artana, C., Cancet, M., Dibarboure, G., Feng, H., Husson, R., Picot, N., Provost, C., and Strub, P. T.: The new CNES-CLS18 global mean dynamic topography, Ocean Sci., 17, 789–808, https://doi.org/10.5194/os-17-789-2021, 2021.

Obligis, E., Desportes, C., Eymard, L., Fernandes, M. J., Lázaro, C., and Nunes, A. L.: Tropospheric Corrections for Coastal Altimetry, in: Coastal Altimetry, edited by: Vignudelli, S., Kostianoy, A. G., Cipollini, P., and Benveniste, J., Springer, Berlin, Heidelberg, 147–176, https://doi.org/10.1007/978-3-642-12796-0_6, 2011.

Ourmières, Y., Zakardjian, B., Beranger, K., and Langlais, C.: Assessment of a NEMO-based downscaling experiment for the North-Western Mediterranean region: Impacts on the Northern Current and comparison with ADCP data and altimetry products, Ocean Model., 39, 386–404, https://doi.org/10.1016/j.ocemod.2011.06.002, 2011.

Passaro, M., Cipollini, P., Vignudelli, S., Quartly, G. D., and Snaith, H. M.: ALES: A multi-mission adaptive subwaveform retracker for coastal and open ocean altimetry | Elsevier Enhanced Reader, Romote Sens. Environ., 145, 173–189, https://doi.org/10.1016/j.rse.2014.02.008, 2014.

Passaro, M., Nadzir, Z. A., and Quartly, G. D.: Improving the precision of sea level data from satellite altimetry with high-frequency and regional sea state bias corrections, Remote Sens. Environ., 218, 245–254, https://doi.org/10.1016/j.rse.2018.09.007, 2018.

Peltier, W. R.: Postglacial variations in the level of the sea: Implications for climate dynamics and solid-Earth geophysics, Rev. Geophys., 36, 603–689, https://doi.org/10.1029/98RG02638, 1998.

Peltier, W. R.: GLOBAL GLACIAL ISOSTASY AND THE SURFACE OF THE ICE-AGE EARTH: The ICE-5G (VM2) Model and GRACE, Annu. Rev. Earth Planet. Sci., 32, 111–149, https://doi.org/10.1146/annurev.earth.32.082503.144359, 2004.

https://doi.org/10.5194/essd-2022-292
Preprint. Discussion started: 29 September 2022

Petrenko, A., Dufau, C., and Estournel, C.: Barotropic eastward currents in the western Gulf of Lion, north-western Mediterranean Sea, during stratified conditions, J. Mar. Syst., 74, 406–428, https://doi.org/10.1016/j.jmarsys.2008.03.004, 2008.

Poisson, J.-C., Quartly, G. D., Kurekin, A. A., Thibaut, P., Hoang, D., and Nencioli, F.: Development of an ENVISAT Altimetry Processor Providing Sea Level Continuity Between Open Ocean and Arctic Leads, IEEE Trans. Geosci. Remote Sens., 56, 5299–5319, https://doi.org/10.1109/TGRS.2018.2813061, 2018.

Poulain, P.-M., Gerin, R., Rixen, M., Zanasca, P., Teixeira, J., Griffa, A., Molcard, A., De Marte, M., and Pinardi, N.: Aspects of the surface circulation in the Liguro-Provençal basin and Gulf of Lion as observed by satellite-tracked drifters (2007-2009), Boll. Geofis. Teor. Ed Appl., 53, 261–279, 2012.

Prandi, P., Poisson, J.-C., Faugère, Y., Guillot, A., and Dibarboure, G.: Arctic sea surface height maps from multi-altimeter combination, Oceanography – Physical, https://doi.org/10.5194/essd-2021-123, 2021.

Pujol, M., Schaeffer, P., Faugère, Y., Raynal, M., Dibarboure, G., and Picot, N.: Gauging the Improvement of Recent Mean Sea Surface Models: A New Approach for Identifying and Quantifying Their Errors, J. Geophys. Res. Oceans, 123, 5889–5911, https://doi.org/10.1029/2017JC013503, 2018.

Pujol, M.-I., Faugère, Y., Taburet, G., Dupuy, S., Pelloquin, C., Ablain, M., and Picot, N.: DUACS DT2014: the new multi-mission altimeter data set reprocessed over 20years, Ocean Sci., 12, 1067–1090, https://doi.org/10.5194/os-12-1067-2016, 2016.

Pujol, M.-I., Dupuy, S., Vergara, O., Sánchez-Román, A., Faugère, Y., Prandi, P., Dabat, M.-L., Dagneaux, Q., Lievin, M., Cadier, E., Dibarboure, G., and Picot, N.: high-resolution Level-3 altimeter DUACS experimental regional product, , https://doi.org/10.48670/moi-00137, 2020a.

Pujol, M.-I., Dupuy, S., Vergara, O., Sánchez-Román, A., Faugère, Y., Prandi, P., Dabat, M.-L., Dagneaux, Q., Lievin, M., Cadier, E., Dibarboure, G., and Picot, N.: high-resolution Level-3 altimeter DUACS experimental regional product (version V02), , https://doi.org/10.24400/527896/a01-2021.003, 2020b.

Qiu, B., Chen, S., Klein, P., Wang, J., Torres, H., Fu, L.-L., and Menemenlis, D.: Seasonality in Transition Scale from Balanced to Unbalanced Motions in the World Ocean, J. Phys. Oceanogr., 48, 591–605, https://doi.org/10.1175/JPO-D-17-0169.1, 2018.

Quartly, G. D., Smith, W. H. F., and Passaro, M.: Removing Intra-1-Hz Covariant Error to Improve Altimetric Profiles of σ^{0} and Sea Surface Height, IEEE Trans. Geosci. Remote Sens., 57, 3741–3752, https://doi.org/10.1109/TGRS.2018.2886998, 2019.

Quilfen, Y. and Chapron, B.: On denoising satellite altimeter measurements for high-resolution geophysical signal analysis, Adv. Space Res., 68, 875–891, https://doi.org/10.1016/j.asr.2020.01.005, 2021.

Raney, R. K.: The delay/Doppler radar altimeter, IEEE Trans. Geosci. Remote Sens., 36, 1578–1588, https://doi.org/10.1109/36.718861, 1998.

https://doi.org/10.5194/essd-2022-292
Preprint. Discussion started: 29 September 2022

Raynal, M., Labroue, S., Moreau, T., Boy, F., and Picot, N.: From conventional to Delay Doppler altimetry: A demonstration of continuity and improvements with the Cryosat-2 mission, Adv. Space Res., 62, 1564–1575, https://doi.org/10.1016/j.asr.2018.01.006, 2018.

Rieu, P., Moreau, T., Cadier, E., Raynal, M., Clerc, S., Donlon, C., Borde, F., Boy, F., and Maraldi, C.: Exploiting the Sentinel-3 tandem phase dataset and azimuth oversampling to better characterize the sensitivity of SAR altimeter sea surface height to long ocean waves, Adv. Space Res., 67, 253–265, https://doi.org/10.1016/j.asr.2020.09.037, 2021.

Rio, M.-H., Pascual, A., Poulain, P.-M., Menna, M., Barceló, B., and Tintoré, J.: Computation of a new mean dynamic topography for the Mediterranean Sea from model outputs, altimeter measurements and oceanographic in situ data, Ocean Sci., 10, 731–744, https://doi.org/10.5194/os-10-731-2014, 2014.

Roblou, L., Lamouroux, J., Bouffard, J., Lyard, F., Le Hénaff, M., Lombard, A., Marsaleix, P., De Mey, P., and Birol, F.: Post-processing Altimeter Data Towards Coastal Applications and Integration into Coastal Models, in: Coastal Altimetry, edited by: Vignudelli, S., Kostianoy, A. G., Cipollini, P., and Benveniste, J., Springer, Berlin, Heidelberg, 217–246, https://doi.org/10.1007/978-3-642-12796-0_9, 2011.

Rocha, C. B., Chereskin, T. K., Gille, S. T., and Menemenlis, D.: Mesoscale to Submesoscale Wavenumber Spectra in Drake Passage, J. Phys. Oceanogr., 46, 601–620, https://doi.org/10.1175/JPO-D-15-0087.1, 2016.

Roinard, H. and Michaud, L.: Jason-3 validation and cross calibration activities (Annual report 2019), CNES, 2019.

Sammari, C., Millot, C., and Prieur, L.: Aspects of the seasonal and mesoscale variabilities of the Northern Current in the western Mediterranean Sea inferred from the PROLIG-2 and PROS-6 experiments, Deep Sea Res. Part Oceanogr. Res. Pap., 42, 893–917, https://doi.org/10.1016/0967-0637(95)00031-Z, 1995.

Sánchez-Román, A., Pascual, A., Pujol, M.-I., Taburet, G., Marcos, M., and Faugère, Y.: Assessment of DUACS Sentinel-3A Altimetry Data in the Coastal Band of the European Seas: Comparison with Tide Gauge Measurements, Remote Sens., 12, 3970, https://doi.org/10.3390/rs12233970, 2020.

Sandwell, D., Schaeffer, P., Dibarboure, G., and Picot, N.: High Resolution Mean Sea Surface for SWOT, 2017.

Sandwell, D. T. and Smith, W. H. F.: Retracking ERS-1 altimeter waveforms for optimal gravity field recovery, Geophys. J. Int., 163, 79–89, https://doi.org/10.1111/j.1365-246X.2005.02724.x, 2005.

Sasaki, H., Klein, P., Qiu, B., and Sasai, Y.: Impact of oceanic-scale interactions on the seasonal modulation of ocean dynamics by the atmosphere, Nat. Commun., 5, 5636, https://doi.org/10.1038/ncomms6636, 2014.

Schaeffer, P., Pujol, I., Faugere, Y., Guillot, A., and Picot, N.: The CNES CLS 2015 Global Mean Sea surface, OSTST, La Rochelle, France, 14, https://ostst.aviso.altimetry.fr/fileadmin/user_upload/tx_ausyclsseminar/files/GEO_03_Pres_OSTST2016_MSS_CNES_CLS2015_V1_16h55.pdf, 2016.

https://doi.org/10.5194/essd-2022-292
Preprint. Discussion started: 29 September 2022

Su, Z., Wang, J., Klein, P., Thompson, A. F., and Menemenlis, D.: Ocean submesoscales as a key component of the global heat budget, Nat. Commun., 9, 775, https://doi.org/10.1038/s41467-018-02983-w, 2018.

SWOT NASA/JPL Project: Surface Water and Ocean Topography Mission (SWOT§) Project Science Requirements Document, 2018.

Taburet, G., Sanchez-Roman, A., Ballarotta, M., Pujol, M.-I., Legeais, J.-F., Fournier, F., Faugere, Y., and Dibarboure, G.: DUACS DT2018: 25 years of reprocessed sea level altimetry products, Ocean Sci., 15, 1207–1224, https://doi.org/10.5194/os-15-1207-2019, 2019.

Thibaut, P., Poisson, J. C., Bronner, E., and Picot, N.: Relative Performance of the MLE3 and MLE4 Retracking Algorithms on Jason-2 Altimeter Waveforms, Mar. Geod., 33, 317–335, https://doi.org/10.1080/01490419.2010.491033, 2010.

Thibaut, P., Piras, F., Poisson, J. C., Moreau, T., Halimi, A., Boy, F., and Guillot, A.: Convergent solutions for retracking conventional and Delay Doppler altimeter echoes, OSTST, Miami, USA, https://ostst.aviso.altimetry.fr/fileadmin/user_upload/IPM_06_Thibaut_LRM_SAR_Retrackers_-_16.9.pdf, 2017.

Thibaut, P., Piras, F., Ollivier, A., Guerou, A., Boy, F., Maraldi, C., Bignalet-Cazalet, F., Dibarboure, G., and Picot, N.: Benefits of the adaptive retracking solution for the Jason-3 GDR-F reprocessing campaing, IEEE IGARSS 2021, Brussels, Belgium, Virtual, https://igarss2021.com/view_paper.php?PaperNum=4121, 2021.

Tourain, C., Piras, F., Ollivier, A., Hauser, D., Poisson, J. C., Boy, F., Thibaut, P., Hermozo, L., and Tison, C.: Benefits of the Adaptive Algorithm for Retracking Altimeter Nadir Echoes: Results From Simulations and CFOSAT/SWIM Observations, IEEE Trans. Geosci. Remote Sens., 59, 9927–9940, https://doi.org/10.1109/TGRS.2021.3064236, 2021.

Tran, N., Philipps, S., Poisson, J.-C., Urien, S., Bronner, E., and Picot, N.: Impact of GDR_D standards on SSB corrections, OSTST, Venice, Italie, http://www.aviso.altimetry.fr/fileadmin/documents/OSTST/2012/oral/02_friday_28/01_instr_processing_I/01_IP1_Tran.pdf, 2012.

Tran, N., Vandemark, D., Zaron, E. D., Thibaut, P., Dibarboure, G., and Picot, N.: Assessing the effects of sea-state related errors on the precision of high-rate Jason-3 altimeter sea level data, Adv. Space Res., 68, 963–977, https://doi.org/10.1016/j.asr.2019.11.034, 2021.

Vergara, O., Morrow, R., Pujol, I., Dibarboure, G., and Ubelmann, C.: Revised Global Wave Number Spectra From Recent Altimeter Observations, J. Geophys. Res. Oceans, 124, 3523–3537, https://doi.org/10.1029/2018JC014844, 2019.

Vergara, O., Morrow, R., Pujol, M.-I., Dibarboure, G., and Ubelmann, C.: Global submesoscale Transition Scale estimation using alongtrack satellite altimetry, Prep, 2022.

Verron, J., Bonnefond, P., Aouf, L., Birol, F., Bhowmick, S. A., Calmant, S., Conchy, T., Crétaux, J.-F., Dibarboure, G., Dubey, A. K., Faugère, Y., Guerreiro, K., Gupta, P. K., Hamon, M., Jebri, F., Kumar, R., Morrow, R., Pascual, A., Pujol, M.-I., Rémy, E., Rémy, F., Smith, W. H. F., Tournadre, J., and Vergara, O.: The Benefits of the Ka-Band as Evidenced from the SARAL/AltiKa Altimetric Mission: Scientific Applications, Remote Sens., 10, 163, https://doi.org/10.3390/rs10020163, 2018.

Vignudelli, S., Kostianoy, A. G., Cipollini, P., and Benveniste, J. (Eds.): Coastal Altimetry, Springer, Berlin, Heidelberg, https://doi.org/10.1007/978-3-642-12796-0, 2011.

Xu, Y. and Fu, L.-L.: The Effects of Altimeter Instrument Noise on the Estimation of the Wavenumber Spectrum of Sea Surface Height, J. Phys. Oceanogr., 42, 2229–2233, https://doi.org/10.1175/JPO-D-12-0106.1, 2012.

Zaron, E. D.: Baroclinic Tidal Sea Level from Exact-Repeat Mission Altimetry, J. Phys. Oceanogr., 49, 193–210, https://doi.org/10.1175/JPO-D-18-0127.1, 2019.

Zaron, E. D. and deCarvalho, R.: Identification and Reduction of Retracker-Related Noise in Altimeter-Derived Sea Surface Height Measurements, J. Atmospheric Ocean. Technol., 33, 201–210, https://doi.org/10.1175/JTECH-D-15-0164.1, 2016.

Acknowledgements

The authors thanks all the people that contributed to this work, including the different CMEMS Model Forecasting Centers (MFCs) that tested the experimental altimeter product and through their feedback contributed to it development. This work was financially and technically supported by the French Space Agency (CNES).

Author contribution

MIP, ML, and PP developed and tested new algorithms and corrections that are applied on the altimeter full rate processing. EC contributed to the preparation of the S3A altimeter databases necessary for this work. SD developed the processing chain necessary for the production and generated the L3 5Hz dataset. MIP, OV, ASR, MLD and QD contributed to the validation of the dataset. MIP interpreted the results and wrote the online documentation. GD, NP and YF supervised the project.

https://doi.org/10.5194/essd-2022-292
Preprint. Discussion started: 29 September 2022

Table 1: Altimeter standards and corrections used for the processing of the different altimeter measurement

	Sentinel-3A	*OSTM/Jason-2*	*Jason-3*	*SARAL/AltiKa*	*Cryosat-2*
Product standard ref	GDR-E				
Orbit	POE-E				
Range processing/retracking	**LR-RMC (with LUT correction)** (Boy et al., 2017; Moreau et al., 2021)	**Adaptive** (Thibaut et al., 2021; Poisson et al., 2018)	**Adaptive** (Thibaut et al., 2021; Poisson et al., 2018)	LRM	SAR & LRM
Noise reduction	-	**HFA adaptive** (Tran et al., 2021)	**HFA adaptive** (Tran et al., 2021)	HFA [Tran 2018]	HFA [Tran 2018] (LRM)
Sea State Bias	Non parametric SSB (Tran et al., 2012)	**2D SSB** (Tran et al., 2021)	**2D SSB** (Tran et al., 2021)	Non parametric SSB	Non parametric SSB
Ionosphere	Dual-frequency altimeter range measurement	Dual-frequency altimeter range measurement	Dual-frequency altimeter range measurement	GIM (Iijima et al., 1999)	
Wet troposphere	From S3A-AMR radiometer	From J3-AMR radiometer Neural Network correction (3 entries), [Fréry et al. in prep]	From J3-AMR radiometer Neural Network correction (3 entries), [Fréry et al. in prep]	Neural Network correction (5 entries) [Picard et al., in prep]	From ECMWF model
Dry troposphere	Model based on ECMWF Gaussian grids				
Combined atmospheric correction	MOG2D High frequencies forced with analysed ECMWF pressure and wind field (Carrère and Lyard, 2003) (operational version used, current version is 3.2.0) + inverse barometer Low frequencies				
Ocean tide	**FES2014b** (Carrere et al., 2016)				
Internal tide	**M2,K1,O1,S2** (Zaron, 2019)**(HRET 7.0)**				
Solid Earth tide	Elastic response to tidal potential(Cartwright and Tayler, 1971; Cartwright and Edden, 1973)				
Pole tide	**From** (Desai et al., 2015) **; Mean Pole Location 2017**				
MSS	**HMP** (Dibarboure and Pujol, 2021)	CNES-CLS-2015 (Schaeffer et al., 2016; Pujol et al., 2018)			
MDT	**CNES_CLS18 (including regional SMDT_MED_2014)** (Mulet et al., 2021; Rio et al., 2014)				

https://doi.org/10.5194/essd-2022-292
Preprint. Discussion started: 29 September 2022

Table 2: Observable wavelengths with the full rate (20Hz or 40Hz) altimeter measurement in the North-Eastern Atlantic ocean [10, 35°W][30, 65°N]. Observable wavelengths estimated from 1Hz measurements over the same area and period are given in () for S3A and J3 missions. (units: km).

Sentinel-3A	OSTM/Jason-2	Jason-3	SARAL/AltiKa	Cryosat-2
35 (65)	55	55 (85)	40	40

Table 3: Mean variance of SSH differences at Jason-3/Jason-3 and Jason-3/Sentinel-3B cross-overs over the year 2019, when no LWE correction is applied or when the LWE correction obtained using the DUACS 1Hz or 5Hz processing is applied on Jason-3. Sentinel-3B is kept as an independent mission for LWE estimation. 1Hz measurements have been used. Only cross-overs within a ten-day interval have been considered. Units are cm².

	No LWE	LWE from DUACS 1Hz processing	LWE from DUACS 5Hz processing
Jason-3/Jason-3	28.40	26.56 (-6.5%)	24.06 (-15.3%)
Jason-3/Sentinel-3B	28.71	27.25 (-5.1%)	26.15 (-8.9%)

Table 4: List of the different physical variables delivered

Name of the variable	Description/Comment
sla_filtered	Sea Level Anomaly Low-pass filtered
mdt	Mean Dynamic Topography
sla_velocity	Anomaly of the geostrophic velocity on the across-track direction
mdt_velocity	Absolute geostrophic velocity on the across-track direction
ocean_tide	Ocean tide signal. Already removed from SLA. Can be reinjected in SLA doing : [uncorrected sla_filtered] = [sla_filtered] + [ocean_tide]
dac	Dynamic Atmospheric Correction. Already removed from SLA. Can be reinjected in SLA doing : [uncorrected sla_filtered] = [sla_filtered] + [dac]
ib_lf	Low Frequency component of the inverse barometer = Low frequency component of the DAC correction (< 20days)
iw	Internal Tide surface signature component. Already removed from SLA. Can be reinjected in SLA doing : [uncorrected sla_filtered] = [sla_filtered] + [iw]
lwe	Long Wavelength Error. Already removed from SLA. Can be reinjected in SLA doing : [uncorrected sla_filtered] = [sla_filtered] - [lwe]

https://doi.org/10.5194/essd-2022-292
Preprint. Discussion started: 29 September 2022

Table 5: Statistics of distance to the coast for the closest altimeter point with a minimal availability rate of 80%. Statistics computed for S3A and J3 measurements retrieved in the 1Hz and 5Hz products over the European coasts.

	Mean (km)	Min (km)	Max (km)	Number of points (count)
S3A 1Hz	10.55	0.55	19.96	478
S3A 5Hz	4.63	0.03	19.93	641
J3 1Hz	11.3	0.05	19.90	259
J3 5Hz	5.8	0.05	19.63	335

Table 6: Spectral parameters of S3A SLA signal over the Gulf Stream and North East Atlantic regions. Mean spectral characteristics over one year and over winter (JFM) and summer (ASO) seasons. measurement over years 2017-2018 were used for these statistics.

	Gulf Steam [42, 66°W] [33, 45°N]			North East Atlantic [10, 34°W] [35, 47°N]		
	Full year	**FMA**	**ASO**	**Full year**	**FMA**	**ASO**
Mesoscale slope	-4.93 +/- 0.08	-4.89 +/- 0.23	-5.03 +/- 0.13	-4.3 +/- 0.19	-3.83 +/- 0.45	-4.74 +/- 0.37
Sub-mesoscale slope	-1.41 +/- 0.17	-1.64 +/- 0.46	-1.32 +/- 0.22	-1.42 +/- 0.12	-1.37 +/- 0.48	-1.49 +/- 0.14
Lt (km)	53.61 +/- 7.36	54.76 +/- 23.29	59.07 +/- 11.19	98.16 +/- 21.24	74.06 +/- 55.94	121.35 +/- 38.38
Noise (cm rms)	4.16	4.27	4.09	4.18	4.33	4.11

https://doi.org/10.5194/essd-2022-292
Preprint. Discussion started: 29 September 2022

Table 7: Inter-comparison of S3A measurements and tide gauge data in the European coasts in terms of variance of the differences between both datasets. The mean distance between tide gauges and the most correlated along-track altimetry points, and the number of total data pairs (altimetry-tide gauge) used in the computation are displayed. The common tide gauge stations for 1Hz and 5Hz products were used. ( ) shows the uncertainties (error bars) computed for variance from the bootstrap method using 10.000 iterations. Finally, the improvement (%) of 5Hz data on the comparison with tide gauges in terms of lower variance of the differences (altimetry-tide gauge), lower mean distance between the most correlated altimetry point and tide gauges, and larger number of available data with respect to 1Hz data are also displayed.

	1Hz	5Hz	Improv 5Hz
Var TG (cm^2)	128 (10)	134 (9)	-
Var ALT (cm^2)	112 (8)	126 (8)	-
Var TG-ALT (cm^2)	61 (6)	58 (5)	-5%
Distance TG (km)	20	19	-5%
Data pairs	2962	3220	+8.7%

Table 8: Same as Table 7, but using J3 measurements

	1Hz	5Hz	Improv 5Hz
Var TG (cm^2)	157 (18)	154 (16)	-
Var ALT (cm^2)	135 (14)	131 (13)	-
Var TG-ALT (cm^2)	70 (11)	58 (8)	-17%
Distance TG (km)	21	20	-5%
Data pairs	1255	1327	+5.7%

https://doi.org/10.5194/essd-2022-292
Preprint. Discussion started: 29 September 2022

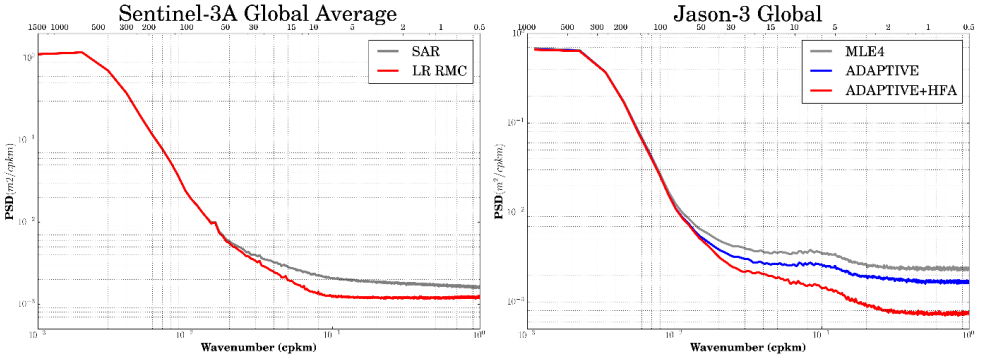

Figure 1: Power spectral density of the SLA along S3A (left) and J3 (right) tracks estimated using different processes. For S3A, conventional SAR (grey) and new LR-RMC (red) processors are presented. For J3, conventional MLE4 (grey), new adaptive (including revised SSB; blue) and new adaptive combined with HFA correction (red) processors are presented.

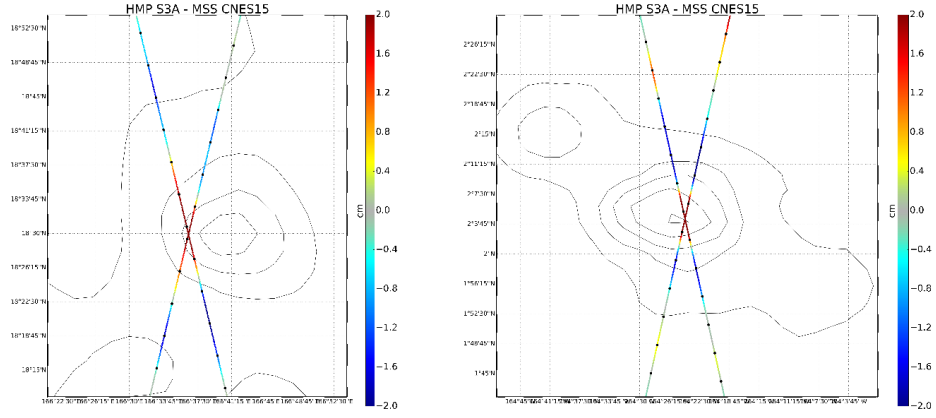

Figure 2: Differences between the full rate (20Hz) S3A HMP and the CNES_CLS15 gridded reference MSS over two seamounts. Bathymetric contours at 1000m intervals are shown as black lines. Black dots illustrate the 1Hz sampling. Unit is cm.

https://doi.org/10.5194/essd-2022-292
Preprint. Discussion started: 29 September 2022

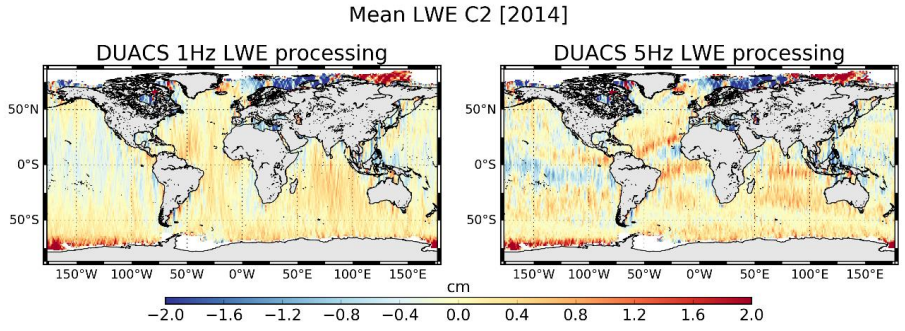

Figure 3: Mean LWE correction for C2 data over year 2014. LWE correction obtained when applying the DUACS 1Hzprocessor (left), and the 5Hz processor (right).

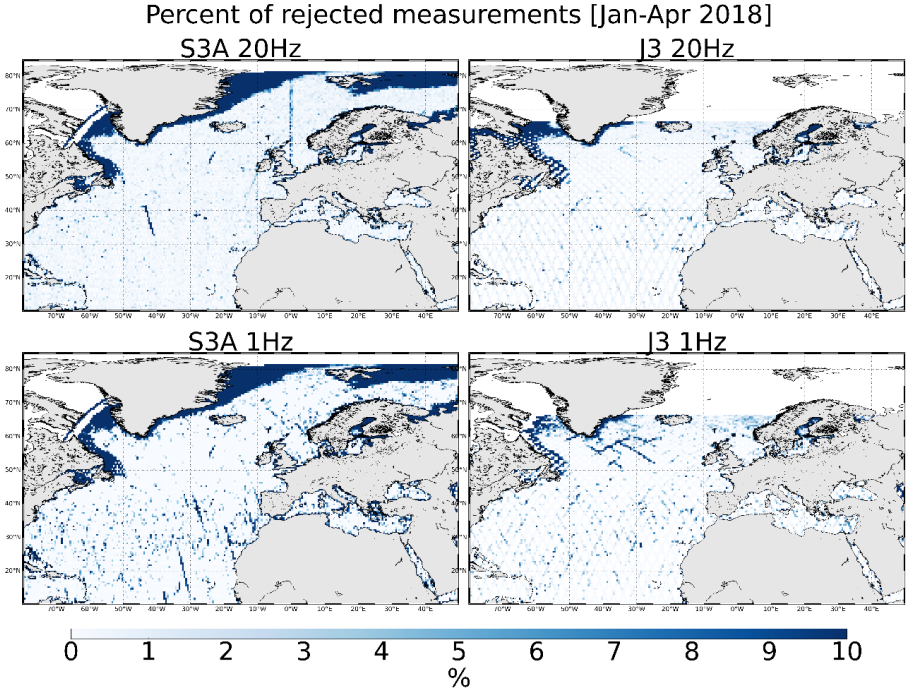

Figure 4: Percentage of rejected measurements for S3A (left) and J3 (right) missions for January-April 2018. Results obtained for 20Hz (top) and 1Hz (bottom) measurements selected with the respective editing strategy.

https://doi.org/10.5194/essd-2022-292
Preprint. Discussion started: 29 September 2022

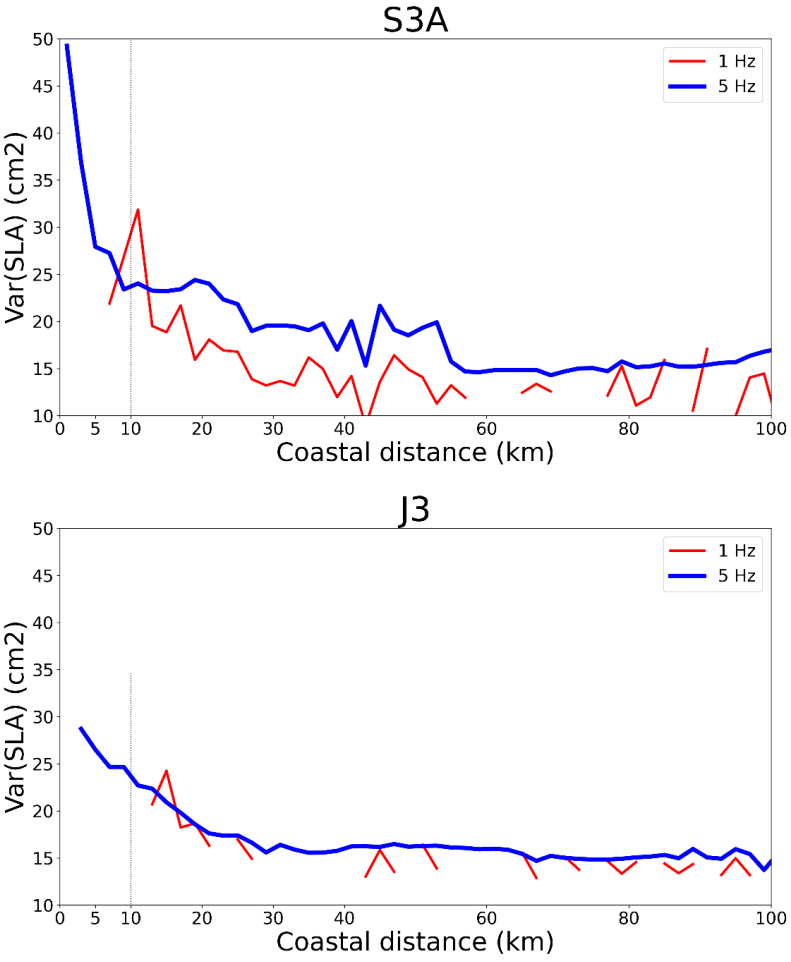

Figure 5: Mean SLA variance evolution as a function of the coastal distance for S3A (top) and J3 (bottom). Only theoretical measurement points with a minimum availability rate of 80% have been considered. Statistics over the Northern Spanish coasts, from 1Hz (red) and 5Hz (blue) products.

https://doi.org/10.5194/essd-2022-292
Preprint. Discussion started: 29 September 2022

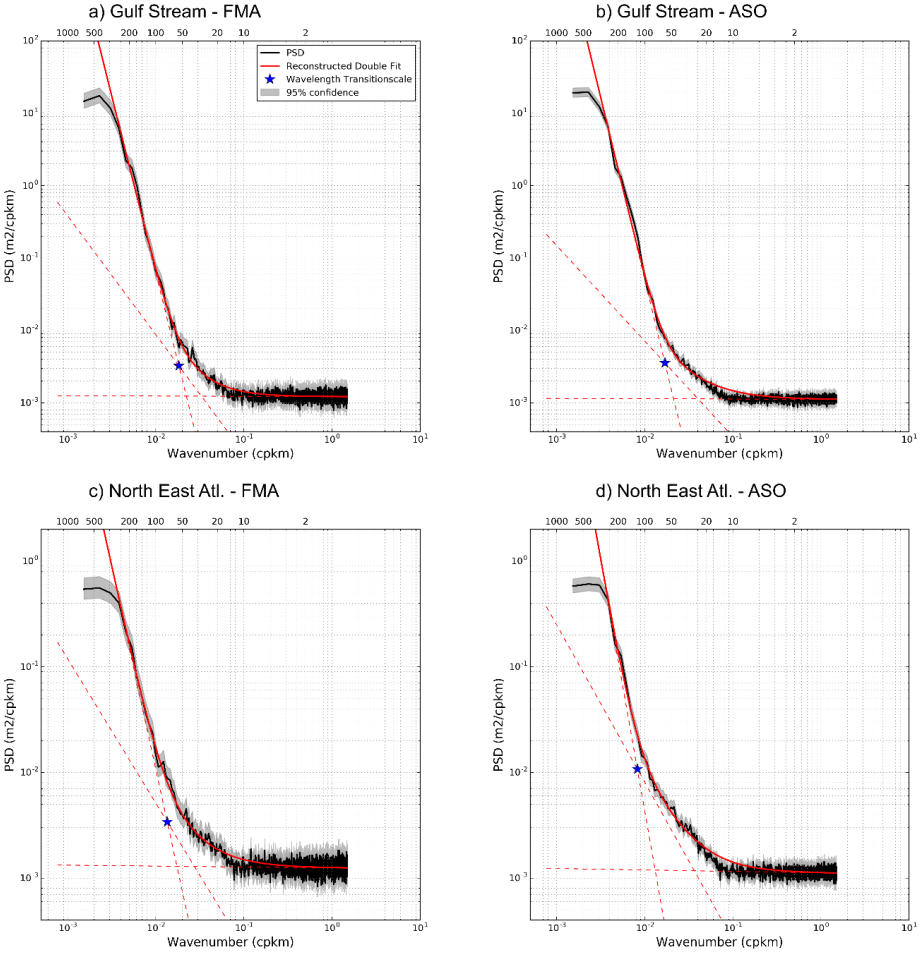

Figure 6: Power spectral density of the SLA along the S3A track in the Gulf Stream domain (top) and North Atlantic domain (bottom). FMA (left) and ASO (right) 2017-2018. The black line shows the true PSD deduced from the signal. The 95% confidence interval is represented by the light grey band centered on the true PSD. The dashed red lines show the 3-slope spectral decomposition. The thick red line shows the theoretical spectrum deduced from the sum of the 3 different slopes. The blue star shows the transition scale (Lt) dividing balanced from unbalanced motions.

https://doi.org/10.5194/essd-2022-292
Preprint. Discussion started: 29 September 2022

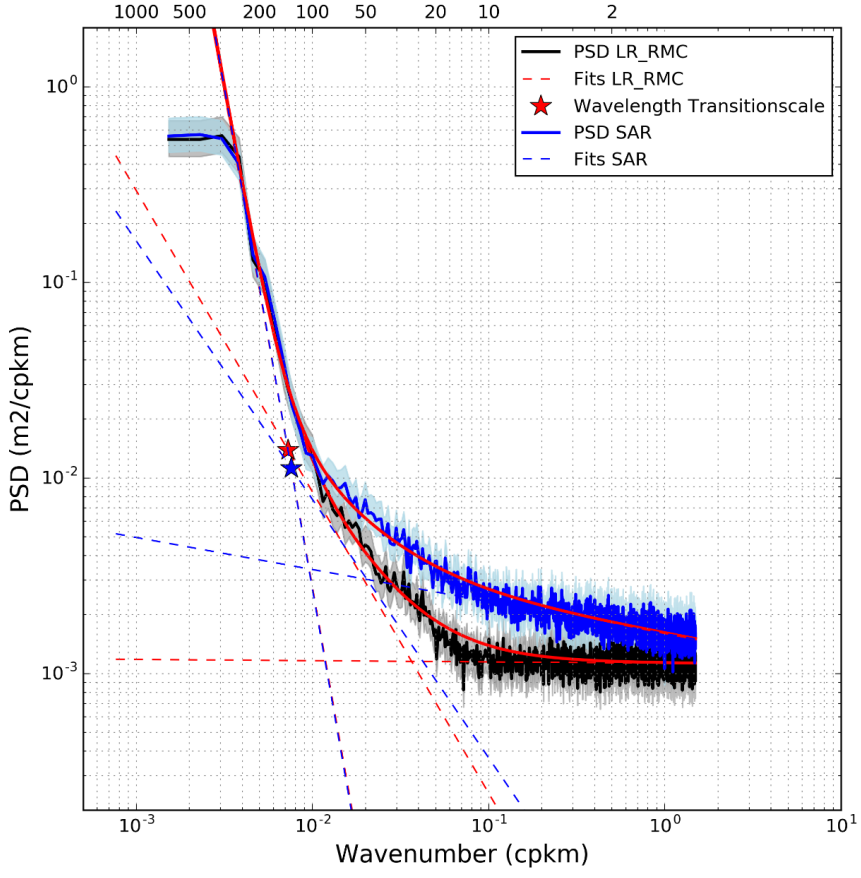

Figure 7: Power spectral density of the SLA along S3A track in the North Atlantic area during the ASO 2017 period. Results obtained with LR-RMC (blue) and SAR (red) processed measurements.

https://doi.org/10.5194/essd-2022-292
Preprint. Discussion started: 29 September 2022

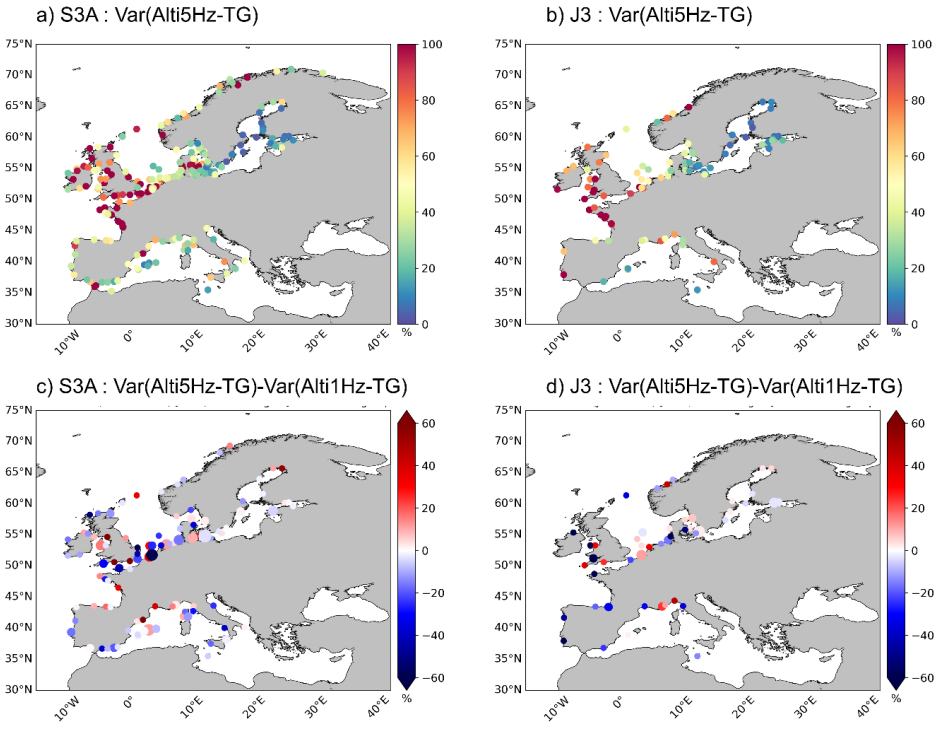

Figure 8: Top : Variance of the differences between S3A (a) or J3 (b) altimeter measurements and TG SLA signal when the 5Hz altimeter product is used. Bottom: difference of the results obtained with the DUACS 1Hz product for S3A (c) and J3 (d). Large dots indicate clusters of neighboring TGs that have been weighted for the computation of global mean statistics. Negative values mean that the SLA differences between altimetry and TGs are lower for the 5Hz products. (Unit: % of the variance of the TG signal).

https://doi.org/10.5194/essd-2022-292
Preprint. Discussion started: 29 September 2022

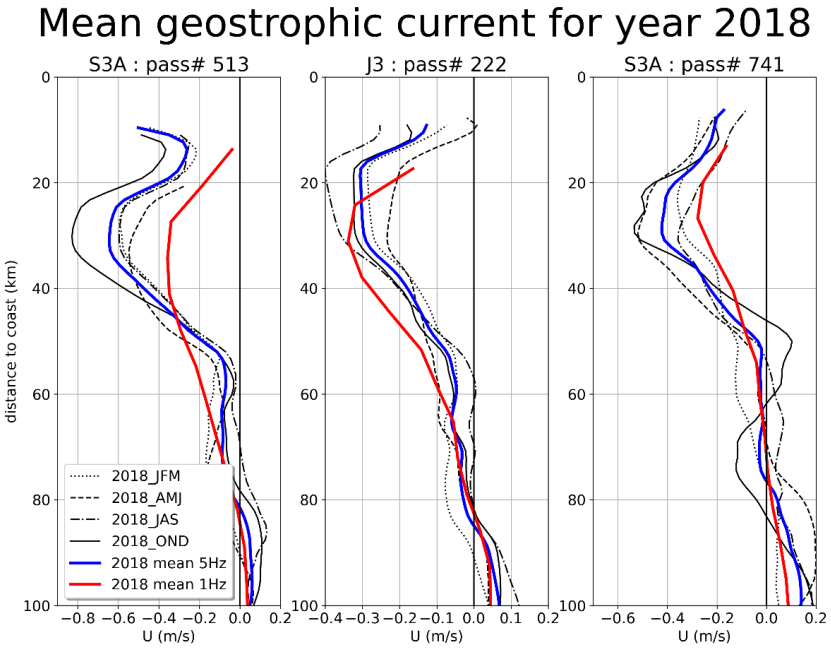

Figure 9: Mean across-track current along the J3 pass #222 (center) and SA pass #513 (left) and #741 (right) crossing the NC. The current is displayed as a function of the distance to the coast. Results obtained using 5Hz product: mean over year 2018 (blue line) and 2018 seasons (black lines). Mean over year 2018 obtained using 1Hz product (red line)